

# Enhancement of Thermoelectric Figure-of-Merit by a Bulk Nanostructuring Approach

By Yucheng Lan, Austin Jerome Minnich, Gang Chen,\* and Zhifeng Ren\*

Recently a significant figure-of-merit ( $ZT$ ) improvement in the most-studied existing thermoelectric materials has been achieved by creating nanograins and nanostructures in the grains using the combination of high-energy ball milling and a direct-current-induced hot-press process. Thermoelectric transport measurements, coupled with microstructure studies and theoretical modeling, show that the  $ZT$  improvement is the result of low lattice thermal conductivity due to the increased phonon scattering by grain boundaries and structural defects. In this article, the synthesis process and the relationship between the microstructures and the thermoelectric properties of the nanostructured thermoelectric bulk materials with an enhanced  $ZT$  value are reviewed. It is expected that the nanostructured materials described here will be useful for a variety of applications such as waste heat recovery, solar energy conversion, and environmentally friendly refrigeration.

where  $S$ ,  $\sigma$ ,  $\kappa$ , and  $T$  are the Seebeck coefficient, the electrical conductivity, the thermal conductivity, and the absolute temperature at which the properties are measured, respectively. The efficiency of a thermoelectric device is directly related to  $ZT$ . For power generation, the efficiency is

$$\eta = \frac{T_h - T_c}{T_h} \frac{\sqrt{1 + Z\bar{T}} - 1}{\sqrt{1 + Z\bar{T}} + T_c/T_h} \quad (2)$$

and for air-conditioning and refrigeration, the coefficient of performance is

$$\text{COP} = \frac{T_c}{T_h - T_c} \frac{\sqrt{1 + Z\bar{T}} - T_h/T_c}{\sqrt{1 + Z\bar{T}} + 1} \quad (3)$$

## 1. Introduction

Thermoelectric materials are capable of directly converting heat into electricity. If a temperature gradient is imposed on a thermoelectric junction, a voltage gradient will form in response via the Seebeck effect, discovered by Thomas Johann Seebeck in 1821. Likewise, a current flow across a thermoelectric junction will produce cooling or heating at the junction via the Peltier effect, discovered by Jean Charles Athanase Peltier in 1834. Solid state thermoelectric devices can be used in a wide range of applications, such as temperature measurement, waste heat recovery, air conditioning, and refrigeration.<sup>[1–11]</sup> Thermoelectric devices have attracted extensive interest for several decades because of their unique features: no moving parts, quiet operation, low environmental impact, and high reliability.<sup>[1–4,7,8,10]</sup> The efficiency of the thermoelectric materials is determined by a dimensionless figure-of-merit ( $ZT$ ), defined as<sup>[1,3,4,12,13]</sup>

$$ZT = (S^2\sigma/\kappa)T \quad (1)$$

where  $T_h$  and  $T_c$  are the hot-end and cold-end temperature of the thermoelectric materials, respectively, and  $\bar{T}$  is the average temperature of  $T_c$  and  $T_h$ . Thus, it is important to use materials with a high  $ZT$  value for practical applications.

The low  $ZT$  value of commercially available thermoelectric materials limits the applications of thermoelectric devices. Metals and metal alloys whose  $ZT$ s are very low ( $ZT \ll 1$ ) can only be applied in thermocouples to measure temperature and radiant energy.<sup>[2]</sup> Semiconducting thermoelectric materials, such as  $\text{Bi}_2\text{Te}_3$  and  $\text{SiGe}$  alloys with  $ZT \approx 1$ ,<sup>[6]</sup> are used commercially in low-power cooling and low-power thermoelectric power generators, such as beverage coolers and laser diode coolers, and power generators in space missions.

To make thermoelectric devices competitive in large-scale and high-power commercial applications, materials with significantly higher  $ZT$  values in the application temperature range are required.<sup>[1,3,4,10,14]</sup> Since the 1960s, much research has been devoted to identifying thermoelectric materials which could satisfy this requirement.

The traditional method to improve  $ZT$  is to discover new thermoelectric materials. Since the thermoelectric effect was discovered, many thermoelectric materials have been identified, such as  $\text{Bi}_2\text{Te}_3$ , skutterudites  $\text{Co}_4\text{Sb}_{12}$ ,  $\text{SiGe}$  alloys,  $\text{PbTe}$ ,  $\text{CsBi}_4\text{Te}_6$ ,<sup>[15]</sup>  $\text{Ti}_9\text{BiTe}_6$ ,<sup>[16]</sup> clathrate  $(\text{Ba},\text{Sr})_8(\text{Al},\text{Ga})_{16}(\text{Si},\text{Ge},\text{Sn})_{30}$ ,<sup>[17]</sup>  $\text{PbTe-PbS}$ ,<sup>[18]</sup> lead antimony silver tellurium based materials<sup>[19,20]</sup> (such as  $\text{AgPb}_m\text{SbTe}_{2+m}$  (LAST),<sup>[19a]</sup>  $\text{Ag}(\text{Pb}_{1-x}\text{Sn}_x)_m\text{SbTe}_{2+m}$  (LASTT),<sup>[19b]</sup>  $\text{Na}_{1-x}\text{Pb}_m\text{Sb}_y\text{Te}_{m+2}$  (SALT),<sup>[19c]</sup> and  $\text{NaPb}_{18-x}\text{Sn}_x\text{SbTe}_{20}$  (SALT)<sup>[19d]</sup>), and  $\text{In}_4\text{Se}_{3-\delta}$ .<sup>[21]</sup> Many of these materials are alloys which help in reducing the phonon thermal conductivity. More thermoelectric materials can be found in other review papers

[\*] Prof. Z. F. Ren, Dr. Y. C. Lan  
Boston College  
Chestnut Hill, Massachusetts 02467 (USA)  
E-mail: renzh@bc.edu  
Prof. G. Chen, A. J. Minnich  
Massachusetts Institute of Technology  
Cambridge, Massachusetts 02139 (USA)  
E-mail: gchen2@mit.edu

DOI: 10.1002/adfm.200901512

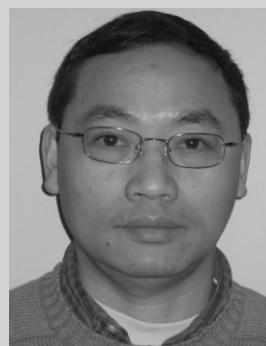
and books.<sup>[6,20,22–24]</sup> Some of the above materials have been incorporated in commercially available devices.

The second method to improve  $ZT$  is via nanostructuring. Experiments show that the thermal conductivity decreases with grain size in the thermoelectric bulk materials.<sup>[13,25–33]</sup> According to Equation 1,  $ZT$  will be increased when the thermal conductivity decreases so long as the power factor,  $S^2\sigma$ , is not strongly reduced. More details are reviewed in the literature.<sup>[4,34]</sup> In the nanostructuring approach, numerous boundaries or interfaces are introduced throughout the thermoelectric materials such that phonons are highly scattered, reducing the thermal conductivity. Of course, for the strategy to be successful the electrical conductivity and Seebeck coefficient should not be significantly affected.

The concept of low-dimensional nanostructured thermoelectric materials was introduced in the 1990s.<sup>[35]</sup> Both an improvement in the power factor ( $S^2\sigma$ ) and a reduction in lattice thermal conductivity are possible in nanostructures. Particularly, theories and experiments indicated that a larger reduction in thermal conductivity can be achieved in nanometer-sized low-dimensional structures as well as bulk nanograined materials, arising from similar boundary and interface phonon-scattering mechanisms.<sup>[27,36–38]</sup> In recent years, many experimental studies have shown that nanostructuring approach is indeed effective in improving  $ZT$ .<sup>[38–42]</sup> The lattice thermal conductivity  $\kappa_l$  has been reduced via the increased phonon scattering of interfaces in one-dimensional nanotubes and nanowires,<sup>[38,43–46]</sup> in two-dimensional superlattices<sup>[35,36,40,41,47–52]</sup> (such as GaAs/AlAs superlattices,<sup>[47a–c]</sup> Bi<sub>2</sub>Te<sub>3</sub>/Sb<sub>2</sub>Te<sub>3</sub> superlattices,<sup>[40]</sup> PbSe<sub>0.98</sub>Te<sub>0.02</sub>/PbTe quantum dot superlattices,<sup>[41]</sup> and SiGe/Si superlattices<sup>[47e,50–52]</sup>) and in nanostructured materials that consist of three-dimensional nanograins (hereafter we also interchangeably call nanostructured materials nanocomposites, defined as agglomerations of nanograins with either different compositions or crystalline structures, or the same material with precipitates or inclusions).<sup>[38,53–58]</sup> The significant enhancement of  $ZT$  in all these nanostructured material systems is believed to result from the reduction of the thermal conductivity by scattering phonons more effectively than electrons at interfaces in superlattices or at grain boundaries in nanostructures.<sup>[36,39–42,53]</sup>

According to Equation 1,  $ZT$  can also be increased by increasing the power factor, rather than by decreasing thermal conductivity. In the literature, there are reports that  $ZT$  has been enhanced by increasing Seebeck coefficient.<sup>[49,59–63]</sup> At first glance, the increasing of power factor in nanostructures may be surprising, since interfacial scattering can reduce the electrical conductivity. However, thermoelectric materials are usually heavily doped and electron mean free path is already very short. As long as the barrier height between interfaces is not too large, the electrical conductivity will not suffer much and can be compensated by increased doping. In fact, the Seebeck coefficient can potentially be improved due to preferential scattering of low-energy electrons at grain boundaries. In addition to the nanostructuring approach, an increase in the power factor can also be achieved in bulk materials through creating sharp features in the density of states, a general principle as predicted.<sup>[63c]</sup>

In this feature article, we mainly focus on the  $ZT$  enhancements achieved in bulk nanocomposites consisting of three-dimensional nanograins. The very small size of the nanograins introduces a



nanomaterials for efficient energy conversions including photovoltaics and thermoelectrics.

**Dr. Z. F. Ren** is a Professor of Physics at Boston College, PhD in Condensed Matter Physics in 1990 from the Institute of Physics, Chinese Academy of Sciences; a fellow of the American Physical Society; a fellow of the American Association for the Advancement of Science; an expert on materials synthesis, characterizations, and applications, especially



**Dr. Gang Chen** is currently the Carl Richard Soderberg Professor of Power Engineering at MIT. He obtained his Ph.D. degree from UC Berkeley in 1993. He was a faculty member at Duke University, University of California at Los Angeles, and moved to MIT in 2001. He has published extensively in the areas of nanoscale energy transport and conversion and nanoscale heat transfer.

high density of grain boundary interfaces in the nanocomposites. These interfaces scatter phonons more strongly than charge carriers and decrease the thermal conductivity. Reviews of other work can be found in the literature for one-dimensional nanowires<sup>[4,38,64,65]</sup> and for two-dimensional superlattices.<sup>[4,11,46,48]</sup>

The higher  $ZT$  of the nanocomposites makes them attractive for cooling and low grade waste heat recovery applications. The materials can also be integrated into segmented thermoelectric devices, which operate at high temperatures, for thermoelectric power generation. In addition to the high  $ZT$  values, the nanocomposites are isotropic and show better mechanical properties than single crystals. They do not suffer from the cleavage problem that is common in ingots made from traditional zone melting techniques, leading to easier device fabrication and system integration and a potentially longer device lifetime.

## 2. Nanocomposite Preparation

In order to produce nanocomposites, thermoelectric nanoparticles are usually prepared first and then assembled into dense bulk solids.

### 2.1. Nanoparticle Preparation

The thermoelectric nanoparticles can be produced by many methods, such as hydrothermal methods,<sup>[66–71]</sup> wet chemical reactions,<sup>[72,73]</sup> and ball-milling.<sup>[27,30,53–58,65,74–84]</sup>

Among these methods, ball-milling is an effective top-down industrial approach to obtain fine particles. Conventional ball-milling has been employed to produce large quantities of fine particles with a size of one to several micrometers. High-energy ball-milling, developed in the 1970s as an industrial process, can create nanoparticles with a size as small as several nanometers.<sup>[85]</sup> It has been proven that high-energy ball-milling is an effective and powerful processing technique to produce large quantities of thermoelectric nanoparticles from ingots in a short time.<sup>[58]</sup> Figure 1a and b shows crystalline ingots and the crystallinity of a p-type  $(\text{Bi,Sb})_2\text{Te}_3$  ingot before ball-milling. The ingot is a bulk single crystal. After ball-milling, nanoparticles can be obtained (Fig. 1c and d).

Besides grinding from crystalline ingots, thermoelectric nanoparticles can also be prepared directly from the individual elements using the high-energy ball-milling method.<sup>[54–58,76,86–88]</sup>

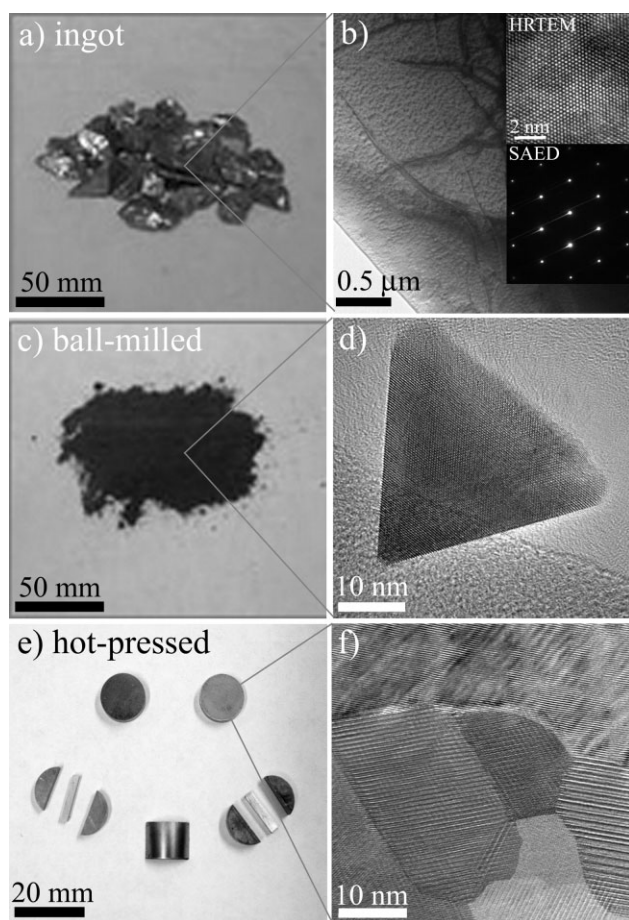


**Figure 1.** a) Optical image of crystalline ingots before ball-milling. b) TEM image of a p-type  $(\text{Bi,Sb})_2\text{Te}_3$  ingot. Insets are HRTEM and SAED of the ingot. c) Optical image of ball-milled nanopowder from ingots. d) HRTEM image of a typical  $(\text{Bi,Sb})_2\text{Te}_3$  nanoflake produced by high-energy ball-milling from ingots. e) Optical image of hot-pressed nanocomposites made from the ball-milled nanopowders shown in (c). f) HRTEM image of several nanograins in a p-type  $(\text{Bi,Sb})_2\text{Te}_3$  nanocomposite produced by the ball-milling and hot-pressing method. The ingots, ball-milled nanopowder, and hot-pressed nanostructured samples shown in (a), (c), and (e) respectively are prepared as described in Ref. [53].

For example, the crystalline  $\text{Bi}_2\text{Te}_3$  nanopowders shown in Figure 1d can be directly synthesized from Bi and Te elements through mechanical alloying.

## 2.2. Bottom-Up Methods to Produce Nanocomposites

In order to obtain thermoelectric nanocomposite materials, the thermoelectric nanoparticles are assembled into a dense solid using various bottom-up methods, such as spark plasma sintering,<sup>[73,77,81–83,89]</sup> cold-pressing,<sup>[74,75,78,90]</sup> sintering,<sup>[30,75,91,92]</sup> hot-pressing,<sup>[53,54,72,79,93–95]</sup> and extrusion methods.<sup>[75,96]</sup>

Among these methods, cold-pressing only mechanically compacts the nanoparticles and thus the density of cold-pressed composites tends to be low, resulting in poor mechanical properties. To improve the mechanical and electrical properties of the composites, the cold-pressing can be followed by a sintering at a certain temperature. However, to reliably create composites with a density of 95–100% of the theoretical value, the hot-pressing method and the spark plasma sintering method are more commonly employed.<sup>[27,53,73,77,97,98]</sup>

Hot-pressing was used to prepare PbSe composites as early as 1960<sup>[99]</sup> and later was employed to produce SiGe polycrystalline materials for NASA space missions. Currently, hot-pressing is a mature technique to produce thermoelectric nanocomposites.<sup>[38]</sup> Most of the nanocomposites with high  $ZT$  reported recently have been prepared using the hot-pressing technique.

The technique to produce nanocomposites can be any combination of a nanoparticle preparation method and a bottom-up assembly method. Based on the various combinations, many nanocomposite preparation methods are possible. Table 1 lists some typical nanocomposite preparation techniques. Under appropriate processing conditions, the produced thermoelectric nanocomposites have a reduced thermal conductivity and a higher  $ZT$ . For example, a peak  $ZT$  of 1.4 is achieved in p-type  $\text{Bi}_x\text{Sb}_{2-x}\text{Te}_3$  nanocomposites produced by a ball-milling and hot-pressing method,<sup>[53]</sup> compared to a peak  $ZT = 1.0$  for the conventional bulk material.

## 2.3. Ball-Milling and Hot-Pressing Method

The ball-milling and hot-pressing method has been employed to produce thermoelectric composites since the 1960s.<sup>[127]</sup> Interested readers are referred to earlier articles on ball-milling and hot-pressing methods in the literature.<sup>[27,87,98,127]</sup> In earlier works, only micrometer-sized particles were obtained from ball-milling. The grain size of these composites varies from several micrometers to one hundred micrometers. The thermal conductivity of the hot-pressed composites was decreased compared with that of the single crystal.<sup>[27,29]</sup> The peak  $ZT$  of SiGe composites consisting of micrometer-sized grains was increased by less than 20%.

Since the invention of high-energy ball-milling, large quantities of nanoparticles can be produced. After hot-pressing, the grains in the nanocomposites still have a size in the nanometer range (Fig. 1f), although grain growth can take place during hot-pressing.

The combination of high-energy ball-milling and hot-pressing is very attractive from a commercial point of view because large quantities of nanopowders can be ball-milled and hot-pressed in a

**Table 1.** Thermoelectric properties of some typical nanocomposites.

Nanocomposites	Carrier Type	ZT [a]	Thermal Conductivity [W m <sup>-1</sup> K <sup>-1</sup> ] [a] [b]	Methods [c] [d]	References
Si <sub>80</sub> Ge <sub>20</sub> B <sub>x</sub>	p	0.95 (0.5) at 800–900 °C	2.5 (5.0)	BM (10–60 hr) + HP(950–1200 °C)	[54]
Si <sub>80</sub> Ge <sub>20</sub> P <sub>2</sub>	n	1.3 (0.93) at 900 °C	2.5 (4.6)	BM + HP(1000–1200 °C)	[56]
Si <sub>63.5</sub> Ge <sub>36.5</sub> P <sub>x</sub>	n	0.128 (0.0937) at RT	3.82 (5.07)	BM + HP	[27]
Si <sub>95</sub> Ge <sub>5</sub>	p	0.95 at 900 °C	5 (10)	BM + HP	[57]
SiP <sub>x</sub>	n	0.7 at 1000 °C	12	BM (1 hr) + HP(>1000 °C)	[100]
Bi <sub>0.5</sub> Sb <sub>1.5</sub> Te <sub>3</sub>	p	0.8 at RT	0.9	BM (300 rpm, 20 hr) + HP(300–550 °C, 30 min)	[32]
(Bi,Sb) <sub>2</sub> Te <sub>3</sub>	p	1.4 (1.0) at 100 °C	1.1 (1.4)	BM + HP	[53]
(Bi,Sb) <sub>2</sub> Te <sub>3</sub>	p	1.3 (1.0) at 75–100 °C	1.25 (1.4)	BM + HP	[55]
(Bi,Sb) <sub>2</sub> Te <sub>3</sub>	p	0.9 at RT	–	BM (400 cycles) + HP(420 °C, 1.2 GPa, 1 hr)	[101]
(Bi,Sb) <sub>2</sub> (Te,Se) <sub>3</sub>	p	0.7–0.9 at RT	1.0–1.5	BM (1200 rpm, 6.5 h) + HP(550 °C, 30 min)	[102]
Bi <sub>2</sub> (Te,Se) <sub>3</sub>	n	1.0 at 100 °C	–	BM + HP	Unpublished
Bi <sub>2</sub> (Te,Se) <sub>3</sub>	n	0.5 at RT	1.0	BM(400 rpm, 10 hr) + HP(500 °C, 4 hr)	[79]
(Bi,Sb) <sub>2</sub> Te <sub>3</sub>	p	1.35 (0.8) at RT	0.6 (1.4)	MS + SPS(510 °C, 10 min)	[103]
(Bi,Sb) <sub>2</sub> Te <sub>3</sub>	p	–	–	BM(800 cycle) + extrusion	[78]
Co <sub>4</sub> Sb <sub>12</sub>	p	0.05 at RT	2.9(4.3)	BM(450 rpm, 15 hr) + SPS(50 MPa, 300 °C, 5 min)	[82]
Co <sub>4</sub> Sb <sub>12</sub>	p	< 0.01 at RT	1.7	CM + HP(100 MPa, 450 °C)	[104]
Co <sub>4</sub> Sb <sub>12</sub>	–	0.11 at 723 K	4.7	CM + HP(100 MPa, 600 °C, 30 min)	[95]
Yb <sub>0.35</sub> Co <sub>4</sub> Sb <sub>12</sub>	n	1.2 at 550 °C	1.52	BM + HP	[105]
Yb <sub>0.19</sub> Co <sub>4</sub> Sb <sub>12</sub>	n	0.26 at RT	2.6	BM + HP(26 PSI, 650 °C, 2 hr)	[106]
Yb <sub>0.29</sub> Co <sub>4</sub> Sb <sub>12</sub>	n	1.3 at 800 K	2.5	MS + SPS(550 °C, 5 min)	[89]
(Ni <sub>0.09</sub> Co <sub>0.91</sub> ) <sub>4</sub> Sb <sub>12</sub>	n	0.75 at RT	3	BM (20–50 hr) + HP(60–160 MPa, 550–780 °C, 1–6 min)	[107]
(Ni <sub>0.08</sub> Co <sub>0.92</sub> ) <sub>4</sub> Sb <sub>12</sub>	–	0.065 at 450 K	5	CM + HP(100 MPa, 450 °C)	[72]
(Ni <sub>0.8</sub> Co <sub>0.2</sub> ) <sub>4</sub> Sb <sub>12</sub>	–	0.1 at RT	3.0	BM(39 hr) + HP(80–160 MPa, 500 °C, 1–5 min)	[108]
Co <sub>4-x</sub> Fe <sub>x</sub> Sb <sub>12</sub>	–	–	–	BM(230 rpm) + sintering	[91]
Fe <sub>1.5</sub> Co <sub>2.5</sub> Sb <sub>12</sub>	p	0.32 at 600 K	2	BM(100 hr) + HP(60 MPa, 550 °C, 2 h)	[109]
SnFe <sub>3</sub> Co <sub>5</sub> Sb <sub>24</sub>	n	0.15 at RT	1.5	BM (100 hr) + HP(60 MPa, 550 °C, 2 h)	[110]
La <sub>x</sub> (Ni,Co) <sub>3</sub> Sb <sub>12</sub>	–	0.12 at RT	3.2	BM(400 rpm, 10 hr) + HP(50 MPa, 600 °C, 2 hr)	[111]
La <sub>1.5</sub> Fe <sub>4</sub> Sb <sub>12</sub>	–	0.41 at 750 K	2	BM (20 hr) + HP(50 MPa, 650 °C, 2 hr)	[112]
La <sub>0.4</sub> FeCo <sub>3</sub> Sb <sub>12</sub>	–	0.04 at RT	3	BM(400 rpm, 14 hr) + HP(70 MPa, 700 °C, 3 hr)	[113]
β-FeSi <sub>2</sub>	–	0.018 at RT	4.5	BM (4 hr) + HP(80–100 MPa, 950 °C, 30 min)	[114]
Fe <sub>0.95</sub> Co <sub>0.05</sub> Si <sub>2</sub>	n	0.18 at 923 K	4.5	BM (300 rpm, 30 min) + HP(50 MPa, 950 °C, 30 min)	[115]
Mg <sub>2</sub> Si <sub>0.4</sub> Sn <sub>0.6</sub>	–	0.13 at 653 K	2.1	BM (600 cycle) + HP	[116]
Mg <sub>2</sub> Si <sub>0.6</sub> Ge <sub>0.4</sub>	p	0.21 at 610 K	4.3	BM (600 cycle) + HP(1 GPa, 500 °C)	[117]
TiNiSn <sub>0.95</sub> Sb <sub>0.05</sub>	–	–	4 (10)	BM (18 hr) + Shock compaction (>5 GPa)	[118]
TiO <sub>x</sub>	n	< 0.025 at RT	2.7–5.7	HP (114 MPa, 1200 °C, 2 min)	[119]
Bi <sub>85</sub> Sb <sub>15</sub>	–	0.3 at 150 K	2.1	BM (236 rpm) + extrusion	[75]
PbTe	n	0.07 at RT	4	BM + SPS(40 MPa, 310–510 °C, 1–10 min)	[77]
GaSb <sub>10</sub> Te <sub>16.5</sub>	p	0.6 at RT	1.2	BM (350 rpm, 5 hr) + SPS(40 MPa)	[120]
Ag <sub>0.8</sub> Pb <sub>22</sub> SbTe <sub>20</sub>	–	1.37 at 673 K	–	BM + SPS(50 MPa, 10 min)	[81]
2 wt%ZrO <sub>2</sub> + β-FeSi <sub>2</sub>	–	0.14 (0.35) at 700 K	4.5 (5.0)	BM (20 hr) + HP(25 MPa, 900 °C, 1 hr)	[121]
2 wt%Y <sub>2</sub> O <sub>3</sub> + β-FeSi <sub>2</sub>	–	0.064 (0.035) at 700 K	4.5 (5.5)	BM(20 hr) + HP(25 MPa, 900 °C, 1 hr)	[122]
5 wt%TiB <sub>2</sub> + β-FeSi <sub>2</sub>	–	0.015 (0.018) at RT	5.2 (4.5)	BM(4 hr) + HP(80–100 MPa, 950 °C, 30 min)	[114]
50% Bi <sub>2</sub> Te <sub>3</sub> + 50% Sb <sub>2</sub> Te <sub>3</sub>	–	1.47 at 450 K	1.1	HS + HP(75 MPa, 350 °C, 15 min)	[71]
10wt% Bi <sub>2</sub> Te <sub>3</sub> nanoparticle + Bi <sub>0.5</sub> Sb <sub>1.5</sub> Te <sub>3</sub> microparticle	–	0.65 at RT	0.55	BM + HP(50 MPa, 310 °C, 30 min)	[123]
10wt% Bi <sub>2</sub> Te <sub>3</sub> nanoparticle + Bi <sub>2</sub> Te <sub>2.85</sub> Se <sub>0.15</sub> microparticle	–	0.83 at 350 K	0.55	BM + HP(50 MPa, 310 °C, 30 min)	[123]
7wt% BN + (Bi <sub>0.2</sub> Sb <sub>0.8</sub> ) <sub>2</sub> Te <sub>3</sub>	–	0.54 (1.0) at RT	1.2 (1.5)	BM (1200 rpm, 5 hr) + HP(425 MPa, 550 °C, 30 min)	[124]
7wt% WO <sub>3</sub> + (Bi <sub>0.2</sub> Sb <sub>0.8</sub> ) <sub>2</sub> Te <sub>3</sub>	–	0.75 (1.0) at RT	1.3 (1.5)	BM (1200 rpm, 5 hr) + HP(425 MPa, 550 °C, 30 min)	[124]
15 wt% nanoplate Bi <sub>2</sub> Te <sub>3</sub> + Bi <sub>2</sub> Te <sub>3</sub>	–	0.39 at RT	1.1	Plasma sintering	[125]
25.4 vol%TiB <sub>2</sub> + B <sub>4</sub> C	–	0.002 (0.01) at 1050 K	16 (9)	BM (10 hr) + HP(35 MPa, 1900 °C, 30 min)	[126]

[a] Data in parentheses are the values of single crystals or of nanocomposites without addition. [b] At room temperature (RT). [c] BM: ball-milling; HS: hydrothermal synthesis; CM: chemical method; MS: melting spinning; HP: hot-pressing; SPS: spark plasma sintering. [d] Experimental details are listed in parentheses.



short time. From a research point of view, this method can prepare many thermoelectric materials with different chemical compositions and doping levels in a short time.

Figure 1e shows several hot-pressed nanocomposites made from the ball-milled nanoparticles. Figure 1f shows the microstructure of a p-type  $(\text{Bi,Sb})_2\text{Te}_3$  nanocomposite made from ball-milling and hot-pressing. The grain size is below  $1\ \mu\text{m}$ . Compared with other bottom-up methods, the ball-milling and hot-pressing method can produce dense bulks with high density. For example, the density of the hot-pressed nanocomposites is higher than 98%<sup>[27]</sup> or even 100%<sup>[53]</sup> of that of the single crystalline material. The hot-pressed nanocomposites are also thermally stable at high temperatures and thermoelectrically isotropic.<sup>[53–55]</sup>

The high-energy ball-milling and hot-pressing method has been employed to prepare many thermoelectric nanocomposites, such as  $\text{Bi}_2\text{Te}_3$ ,<sup>[32,53,55,79]</sup>  $\text{SiGe}$  alloys,<sup>[54,56,57]</sup> and skutterudite  $\text{CoSb}_3$ .<sup>[105,107,108]</sup> Table 1 summarizes some reported thermoelectric nanocomposites prepared by the ball-milling and hot-pressing method.

## 2.4. Chemical Synthesis and Spark Plasma Sintering Method

Besides the ball-milling and hot-pressing method, some nanocomposites have been produced by the chemical synthesis and spark plasma sintering method. In this method, the thermoelectric nanoparticles are firstly synthesized by a chemical method. The size distribution, nanoparticle shape, and quality of the nanoparticles can be finely tuned.<sup>[128]</sup> After spark plasma sintering, fully dense nanocomposites are produced.

Hot-press is a pressure-assisted sintering process, in which a direct current or alternating current produces a high temperature to heat the samples. Spark plasma sintering is another kind of pressure-assisted sintering process, in which a pulsed direct current produces spark discharges to heat samples under high pressure. Both techniques have successfully produced fine-grained thermoelectric bulk materials with high density.

## 3. Microstructures and Thermoelectric Properties of Nanocomposites

The microstructures created during the fabrication process affect the phonon transport and electron transport in the nanocomposites, altering the thermal conductivity, electrical conductivity, and Seebeck coefficient, and hence changing  $ZT$ . Below we review the microstructures of some thermoelectric nanocomposites in detail, showing how the microstructures affect thermoelectric properties of the nanocomposites.

### 3.1. $\text{Bi}_2\text{Te}_3$ Nanocomposites

$\text{Bi}_2\text{Te}_3$  is the most widely used thermoelectric materials near room temperature, and has great commercial applications in refrigeration and waste heat recovery up to  $200\ ^\circ\text{C}$ . The maximum  $ZT$  of the commercial  $\text{Bi}_2\text{Te}_3$  ingots remained at about 1.0 for many years. The peak  $ZT$  of  $\text{Bi}_2\text{Te}_3$  nanocomposites has recently been enhanced to 1.3–1.4 at about  $100\ ^\circ\text{C}$ .<sup>[53,55]</sup>

#### 3.1.1. p-type $\text{Bi}_x\text{Sb}_{2-x}\text{Te}_3$ Nanocomposites

Nanostructured p-type  $\text{Bi}_x\text{Sb}_{2-x}\text{Te}_3$  is the first material system in which an enhanced  $ZT$  was reported.<sup>[53]</sup> Using the ball-milling and hot-pressing approach,  $ZT$  is increased by 30–40% compared with the starting crystalline ingots.<sup>[53,55]</sup>

The nanoparticles are produced by ball-milling crystalline ingots. High-energy ball-milling grinds the crystalline ingots into nanocrystals with size ranging from 5 to 50 nm, with an average size of about 20 nm. The milled nanoparticles are very good crystals with clean surfaces (Fig. 1d), and no nanoprecipitates or amorphous nanoregions were observed in the nanoparticles.

During hot-pressing at high temperature, the nanoparticles are compressed into a solid nanocomposite bulk. The final nanocomposites consist of crystalline nanograins. Statistical analysis of thousands of nanograins (Fig. 2b) shows that the majority of the nanograins have a diameter below  $1.0\ \mu\text{m}$ , with 12% of the nanograins having a diameter of 0–20 nm and about 5% of the nanograins having a diameter of 20–40 nm. Some nanograins are bigger, with a diameter of several hundred nanometers (Fig. 2a), while some are very small, with a diameter of several nanometers (Fig. 1d). The grains with a wide size distribution, as shown in Figure 2b, scatter phonons with a variety of mean free paths (a function of the phonon velocity and phonon wavelength) comparable to or greater than the grain size, reducing the thermal conductivity.

High-resolution transmission electron microscope (HRTEM) images indicate that the grain boundaries are high angle boundaries with random orientation. Selected area electron diffraction (SAED) shows that the grains are single crystals. The

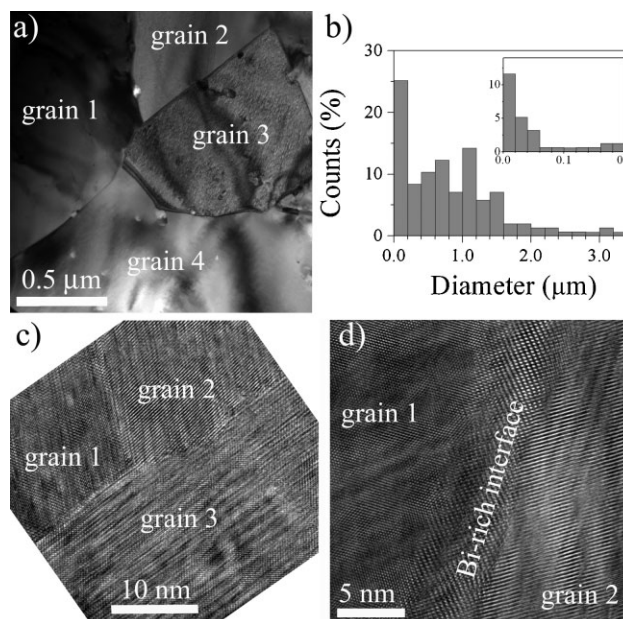


**Figure 2.** a) BF-TEM image of multi-grains and b) grain-size distribution. HRTEM images of c) clean grain boundaries and d) an interface region between two grains in a p-type  $\text{Bi}_x\text{Sb}_{2-x}\text{Te}_3$  nanocomposite. Reproduced with permission from Ref. [129]. Copyright 2009, American Chemical Society.

adjacent grains with random orientation scatter phonons effectively.

In addition to the clean boundaries between grains shown in Figure 2c, some grains in the nanocomposite are surrounded by nanometer thick interface regions (Fig. 2d). The interface region is slightly bismuth-rich,  $1.0 \pm 0.5$  at% higher than that of the grains.<sup>[129]</sup> This bismuth-rich region builds up charges and thus increases the hole concentration in the grains. At the same time, the interface region also scatters phonons. Therefore, the bismuth-rich interface region blocks phonon transport while favoring charge-carrier transport.

Besides the unique grain structures in the nanocomposites, most of the individual nanograins have abundant microstructural defects, which also scatter phonons. Usually there are many three-dimensional nanoprecipitates embedded in the nanograins, as shown in Figure 3a–d. In  $\text{Bi}_x\text{Sb}_{2-x}\text{Te}_3$  nanocomposites, at least four kinds of nanoprecipitates are observed in the crystalline nanograins. A common type of nanoprecipitates is an antimony-rich nanoprecipitate (Fig. 3a). There are no obvious boundaries between the nanoprecipitates and nanograin matrix, with no obvious lattice distortion between them. The lattice is continuous and the fringe spacing almost the same. In the HRTEM images, the nanoprecipitates are brighter than the surrounding crystalline matrix. Another type of nanoprecipitate is a nanodot with an orientation twisted from that of the matrix (Fig. 3b). The chemical composition of the nanodot is the same as that of the surrounding matrix. The third type of nanoprecipitate (Fig. 3c) is also twisted from the surrounding matrix and is also antimony rich. This type of nanoprecipitate is the combination of type-one and type-two nanoprecipitates. The fourth type is a pure tellurium nanodot (Fig. 3d). These polygonal tellurium precipitates are easily identified from the other three types of irregular nanoprecipitates. The diameter of the nanoprecipitates is smaller than 150 nm and their concentration increases with decreasing size (Fig. 3e).

The nanoprecipitates described above are very similar to those observed in  $\text{Ag}_{1-x}\text{Pb}_x\text{SbTe}_{m+2}$  alloys.<sup>[19]</sup> It is believed that the nanoprecipitates are responsible for the ZT enhancement in those alloys. Experiments have shown that the nanometer-sized precipitates embedded in a crystalline host, such as 30–40 nm Pb or Au metal in crystalline PbTe samples, can increase thermoelectric power and reduce thermal conductivity.<sup>[42,60]</sup> In the  $\text{Bi}_x\text{Sb}_{2-x}\text{Te}_3$  nanocomposites, it is expected that these nanoprecipitates will scatter phonons and reduce the thermal conductivity.

Nanoprecipitates with different chemical compositions are expected to scatter both electron and phonons effectively. These nanoprecipitates increase the carrier concentration in the nanograins. Hall effect measurements at room temperature indicate that the hole concentration of the nanocomposites ( $p = 2.5 \times 10^{19} \text{ cm}^{-3}$ ) is about 39% higher than that of the ingots ( $p = 1.8 \times 10^{19} \text{ cm}^{-3}$ ). The increased carrier concentration is partly due to the nanoprecipitates and partly due to the nanointerfaces between nanograins.

All of the grain boundaries, nanointerfaces between nanograins, and nanoprecipitates affect the transport of electrons and phonons. More discussions of the interfacial structure effects are available in the literature.<sup>[130]</sup>

Besides the nanoprecipitates, there are two-dimensional, one-dimensional, and zero-dimensional defects in the nanograins of the nanocomposites.<sup>[129]</sup> TEM investigation indicates that stacking

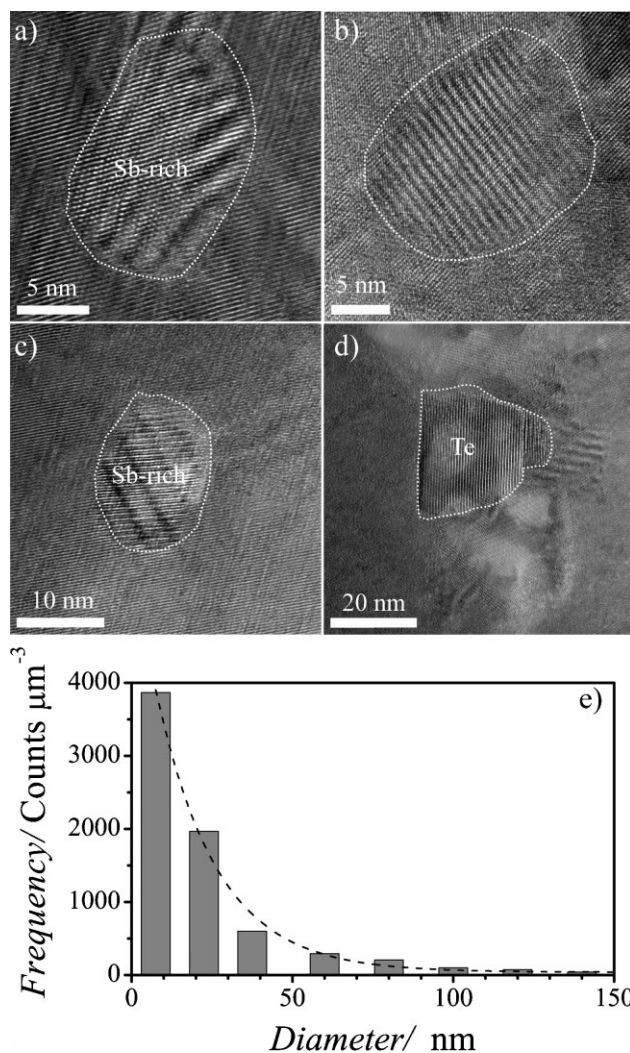


**Figure 3.** Nanoprecipitates embedded in the nanograins of  $\text{Bi}_x\text{Sb}_{2-x}\text{Te}_3$  nanocomposite. HRTEM images of a) an antimony-rich precipitate without boundary, b) a nanoprecipitate with twisted boundary while with the same chemical composition of the surrounding matrix, c) an antimony-rich nanoprecipitate with twisted boundary, and d) a tellurium nanoprecipitate with high-angle boundary. e) The nanoprecipitate size distribution. Reproduced with permission from Ref. [129]. Copyright 2009, American Chemical Society.

faults exist in the nanograins. The threading dislocation concentration is  $\sim 10^{11} \text{ cm}^{-2}$  in nanograins, at least ten times higher than that in the crystalline ingots ( $\sim 5 \times 10^9 \text{ cm}^{-2}$ ). The point defect concentration in nanograins is two to three orders of magnitude higher than that in the ingot. Structural modulations are also observed in the nanograins even though the concentration is almost the same as that in the ingots. All these defects would scatter phonons more effectively and decrease the thermal conductivity of the nanocomposites.

p-type  $\text{Bi}_x\text{Sb}_{2-x}\text{Te}_3$  nanoparticles can also be produced from the individual elements directly through mechanical alloying during high-energy ball-milling. Mechanical alloying can synthesize  $\text{Bi}_x\text{Sb}_{2-x}\text{Te}_3$  nanoparticles with single phase (Fig. 4a) from Bi, Sb and Te. The size of the synthesized nanoparticles is about 5–20 nm with an average size of about 10 nm. The crystalline quality of the



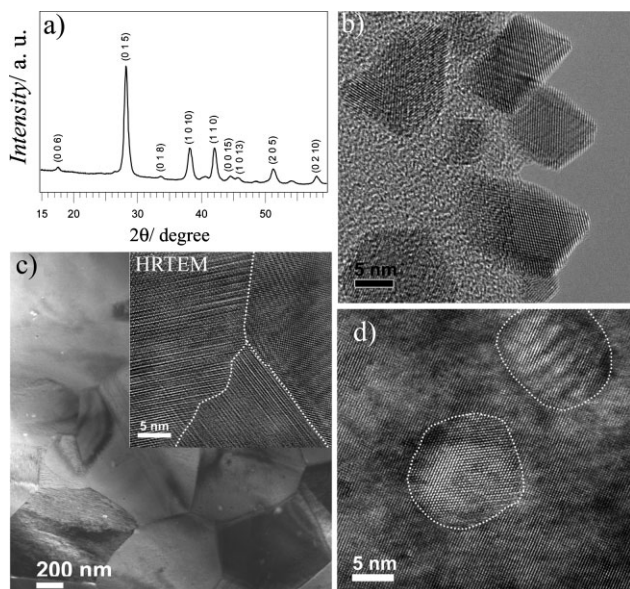


**Figure 4.** a) XRD pattern and b) HRTEM image of mechanically alloyed  $\text{Bi}_x\text{Sb}_{2-x}\text{Te}_3$  nanopowders from the chemical elements. c) BF-TEM image and d) HRTEM image of nanocomposites made from nanoparticles shown in (b). The white dots outline the grain boundaries or nanoprecipitates embedding in the nanograins. Reproduced with permission from Ref. [55]. Copyright 2008, American Chemical Society.

alloyed nanoparticles from the elements is almost the same as that obtained from ingots (Fig. 4b).

It is reported that trace amounts of Sb and Te phases are observed in ball-milled  $\text{Bi}_x\text{Sb}_{2-x}\text{Te}_3$  nanopowders although  $\text{Bi}_x\text{Sb}_{2-x}\text{Te}_3$  single phase is obtained after hot-pressing.<sup>[101]</sup> The unalloyed Sb and Te impurity could be due to insufficient milling time or insufficient transfer energy of ball-milling. If the transfer energy is not high enough, the ball-milling will only grind and mix the elements, not create alloyed nanoparticles.

The microstructure of the nanocomposite made from the elements is very similar to that of the nanocomposite made from ingots. The nanograin size is in the sub-micrometer range and the nanocomposites are densely packed (Fig. 4c). Compared with the starting mechanically alloyed nanopowders (Fig. 4b), the nanograins in nanocomposites grow to larger sizes after hot-pressing (Fig. 4c). Detailed TEM studies indicate that the nanoprecipitates are also formed and embedded inside the  $\text{Bi}_x\text{Sb}_{2-x}\text{Te}_3$  nanograins (Fig. 4d), very similar to the hot-pressed nanocomposites made from the ingots (Fig. 3a–d).

These unique microstructures (shown in Figs. 2–4) affect the thermoelectric properties of the nanocomposites. In Figure 5, we compare the transport properties of three samples: the hot-pressed nanocomposite made from elements, the hot-pressed nanocomposite made from crystalline ingots, and the crystalline ingot itself.

The thermal conductivities of both nanocomposites are significantly lower than that of the ingot because of abundant grain boundaries in the nanocomposites, and the thermal conductivities of both nanocomposites increase more slowly with increasing temperature than does the thermal conductivity of the ingot (Fig. 5a). Comparing the properties of the nanocomposite made from elements with that made from ingot, the thermal

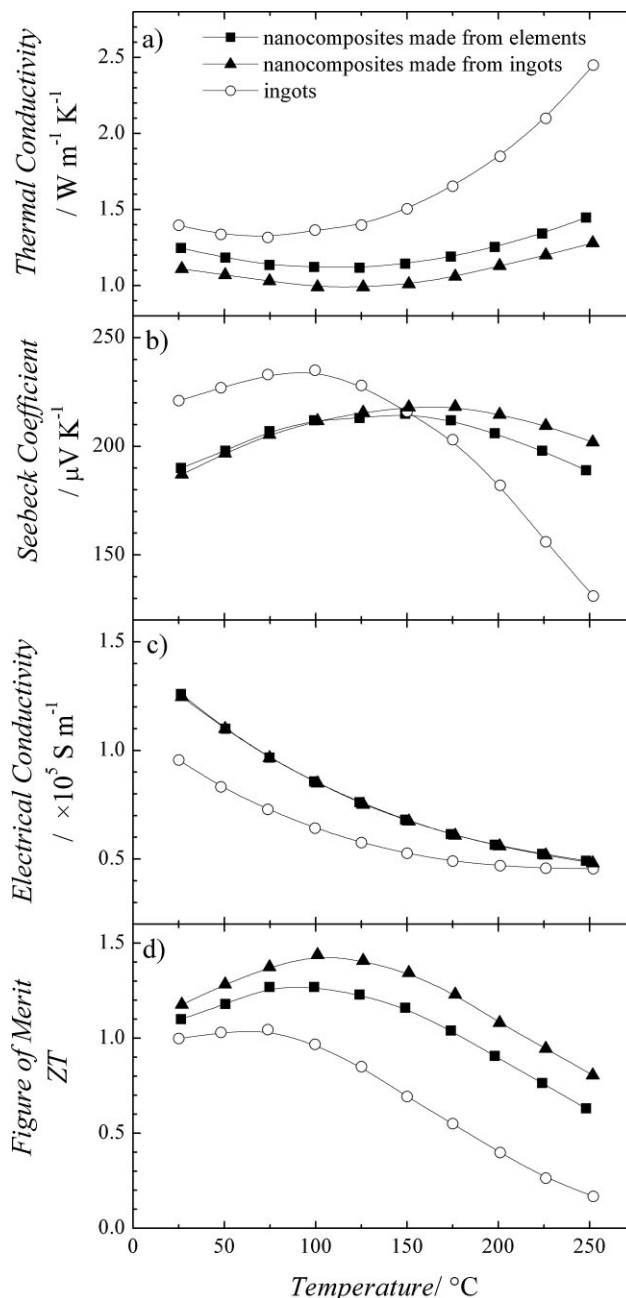


**Figure 5.** a) Thermal conductivity, b) Seebeck coefficient, c) Electrical conductivity, and d) ZT dependence on temperature of hot-pressed  $\text{Bi}_x\text{Sb}_{2-x}\text{Te}_3$  nanocomposites made from elements (filled squares), made from ingots (filled triangles), in comparison with a commercial ingot (open circles). Reproduced with permission from Ref. [55]. Copyright 2008, American Chemical Society.

conductivity of the nanocomposite made from elements is systematically higher than that of the nanocomposite made from ingot. The difference is probably due to lack of some trace amount of elements that were used in the ingot process and to some structural differences.

The Seebeck coefficient (Fig. 5b) of both nanocomposites is lower than that of the crystalline ingot sample below 150 °C but is

higher above 150 °C. The smaller Seebeck coefficient near room temperature is due to a higher carrier concentration, while the larger Seebeck coefficient at higher temperatures is due to the suppression of minority carrier (electron) excitation in heavily doped samples.

The electrical conductivity of the nanocomposites is always higher than that of the crystalline ingots (Fig. 5c) because of the higher carrier concentration ( $2.9 \times 10^{19} \text{ cm}^{-3}$  for nanocomposites and  $1.8 \times 10^{19} \text{ cm}^{-3}$  for the ingots at room temperature). Here the nanoprecipitates embedded in the nanograins and nanointerfaces between nanograins should contribute to the increase of the electrical conductivity. The enhancement of electrical conductivity is very important to improve *ZT* of nanocomposites. Since the 1960s, much work has been carried out in low dimensional composites, and *ZT* could not be increased because of the decrease of electrical conductivity. Although phonons are scattered greatly by the grain boundaries, resulting in a decrease in thermal conductivity, electrons are also scattered by the grain boundaries, resulting in a decrease in electrical conductivity. According to Equation 1, *ZT* increases or decreases depending on the relative values of thermal conductivity and electrical conductivity when the Seebeck coefficient is a constant.

The nanocomposite made from ingots has a power factor comparable to that of the crystalline ingot below 100 °C but higher above 100 °C. The nanocomposites made from elements have a slightly lower power factor than that made from the ingots.

According to Equation 1, *ZT* should be enhanced because the thermal conductivity decreases significantly while the electrical conductivity increases and Seebeck coefficient changes only slightly. Figure 5d shows the temperature dependence of *ZT* for the hot-pressed nanocomposites made from elements and from ingots, in comparison with that of the commercial ingots. The peak *ZT* values shift to a higher temperature and remain significantly higher than that of the ingots at all temperatures. The peak *ZT* values of the hot-pressed nanocomposites made from elements and ingots are about 1.3 and 1.4 at 100 °C, respectively, both of which are significantly higher than that of the best ingots (*ZT* ≈ 1.0).

The *ZT* value of the ingots starts to drop above 75 °C and is below 0.25 at 250 °C, whereas the nanocomposites are still higher than 0.6 at 250 °C. The good *ZT* at high temperatures is very important for power generation applications, since there are no other materials with a similar high *ZT* in this temperature range of 25–250 °C.

Using the ball-milling and hot-pressing method, other groups also prepared p-type  $\text{Bi}_x\text{Sb}_{2-x}\text{Te}_3$  nanocomposites<sup>[27,32,101,131–135]</sup> and p-type  $(\text{Bi,Sb})_2(\text{Te,Se})_3$  nanocomposites.<sup>[102]</sup> *ZT* is less than 1.0 and lower than that of the crystalline ingots. There are many reasons that *ZT* could decrease, with the most likely cause being a decrease in electrical conductivity. The electrical conductivity of the nanocomposites is very sensitive to oxygen, moisture, and other environmental factors. The decrease in electrical conductivity cancels the contribution of the decreased thermal conductivity to *ZT*. In order to achieve good electrical conductivity, the thermoelectric materials should be kept away from oxygen and moisture.

Using a ball-milling and hot-pressing method, p-type  $(\text{Bi,Sb})_2\text{Te}_3$  composites composed of 100-μm particles and 15–30-nm  $\text{Bi}_2\text{Te}_3$  nanoparticles were also obtained.<sup>[123]</sup> A peak *ZT* of 0.83 was achieved.

p-type  $(\text{Bi,Sb})_2\text{Te}_3$  nanocomposites have also been prepared by other methods, such as by the shear extrusion method at high

temperatures from ball-milled powder,<sup>[78]</sup> by the hot-pressing method from hydrothermally synthesized nanoparticles,<sup>[71]</sup> and by melting spinning and spark plasma sintering.<sup>[103]</sup> More nanocomposites and detailed information are listed in Table 1. Among them, one interesting nanocomposite is p-type  $\text{Bi}_2\text{Te}_3$  nanocomposite with layered nanostructure.<sup>[103]</sup> The nanocomposite bulk consists of  $\text{Bi}_2\text{Te}_3$  nanolayers with thickness of 10–40 nm, similar to the structure of  $\text{Bi}_2\text{Te}_3/\text{Sb}_2\text{Te}_3$  superlattices prepared by molecular-beam epitaxy.<sup>[40]</sup> The large number of interfaces reduce the lattice thermal conductivity extraordinarily to  $0.58 \text{ W m}^{-1} \text{ K}^{-1}$ . A peak *ZT* of 1.35 is obtained at 300 K in the nanocomposite, an increase of 73% over the *ZT* of the ingot.

### 3.1.2. n-type $\text{Bi}_2\text{Te}_{3-y}\text{Se}_y$ Nanocomposites

n-type  $\text{Bi}_2\text{Te}_{3-y}\text{Se}_y$  nanocomposites can also be prepared using the same method. n-type  $\text{Bi}_2\text{Te}_{3-y}\text{Se}_y$  single crystalline nanoparticles have been obtained by ball-milling from ingots or elements. The microstructure of n-type  $\text{Bi}_2\text{Te}_{3-y}\text{Se}_y$  nanocomposites is very similar to that of p-type  $\text{Bi}_x\text{Sb}_{2-x}\text{Te}_3$  nanocomposites. The thermal conductivity, electrical conductivity, and Seebeck coefficient are decreased compared with that of the n-type crystalline ingots (Fig. 6). The peak *ZT* is close to 1.0. More work on the n-type  $\text{Bi}_2\text{Te}_{3-y}\text{Se}_y$  nanocomposites is currently underway to preserve the power factor.

n-type  $\text{Bi}_2\text{Te}_3$  nanocomposites have also been prepared by other groups using the ball-milling and hot-pressing method.<sup>[79,80,136,137]</sup> The grain size of these nanocomposites varies from nanometers to micrometers. The reported peak *ZT* values are less than 1.0.

## 3.2. SiGe Alloy Nanocomposites

Silicon–germanium alloys have been the primary thermoelectric materials in power generation devices operating in the temperature range of 600–1000 °C,<sup>[3,6]</sup> having long been used in radio-isotope thermoelectric generators (RTGs) for deep-space missions to convert radio-isotope heat into electricity.<sup>[3,6]</sup> SiGe alloys also hold promise in terrestrial applications such as waste heat recovery.<sup>[12,13,138]</sup>

Since the 1960s, efforts have been made to improve the *ZT* of SiGe alloys,<sup>[13,27,138–142]</sup> with the peak *ZT* of n-type SiGe reaching 1 at 900–950 °C<sup>[13,27,138–142]</sup> and 0.65 in p-type SiGe alloys.<sup>[28,29,141]</sup> Through a ball-milling and hot-pressing method, a significant improvement in *ZT* was achieved in p-type SiGe nanocomposites, with a peak value about 0.95 at 900–950 °C.<sup>[54]</sup> The *ZT* improvement was about 90% over that of RTG samples (peak *ZT* = 0.5), and 50% over the previous highest record (0.65).<sup>[28]</sup> A peak *ZT* of about 1.3 at 900 °C was also achieved in n-type SiGe nanocomposites using the ball-milling and hot-pressing method.<sup>[56]</sup>

### 3.2.1 p-type $\text{Si}_{80}\text{Ge}_{20}$ Nanocomposites

SiGe alloys consisting of micrometer-sized particles have been prepared using the ball-milling and hot-pressing method since the 1960s.<sup>[29]</sup> A 20% increase in *ZT* of p-type SiGe with an optimal grain size in the 2–5-μm range has been reported.<sup>[29]</sup> Presently the typical grain size is 1–10 μm in the RTG samples used for NASA space missions. In heavily doped SiGe alloys, the mean free paths of electrons and phonons are different, with electrons having an



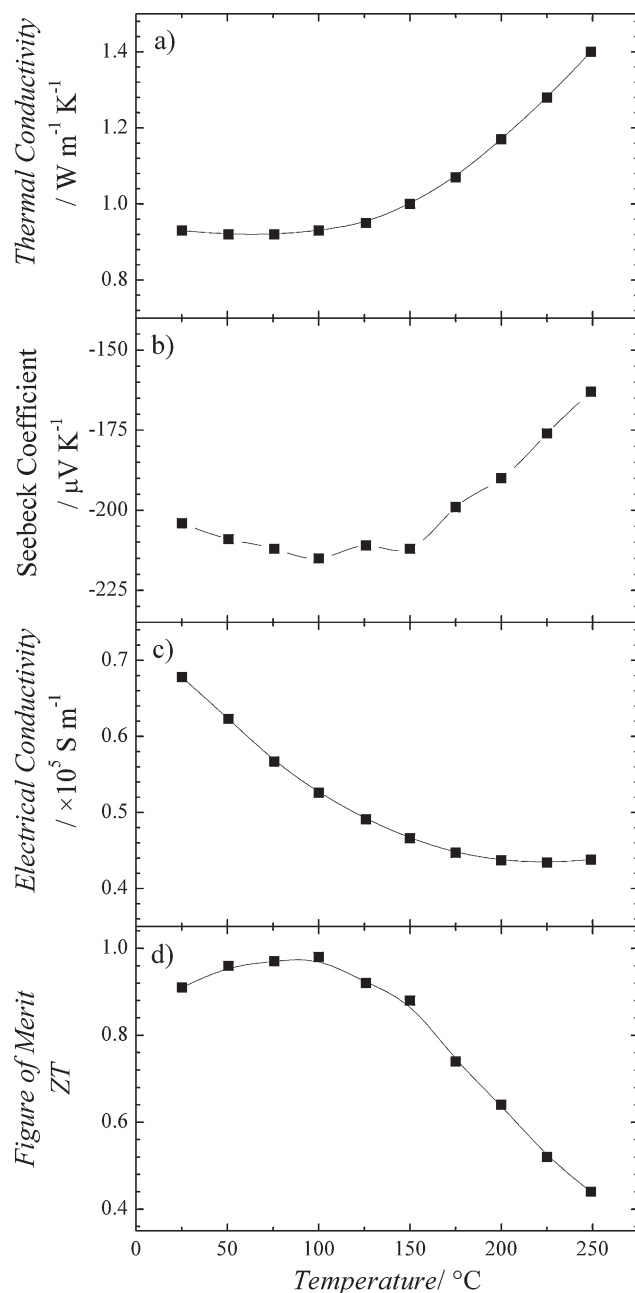


**Figure 6.** Thermoelectric properties of hot-pressed  $\text{Bi}_2\text{Te}_{3-y}\text{Se}_y$  nanocomposites. a) Thermal conductivity, b) Seebeck coefficient, c) electrical conductivity, and d)  $ZT$  dependence of temperature. The nanocomposites are prepared as described in Ref. [53].

average mean free path of about 5 nm and phonons having an average mean free path of 200–300 nm at room temperature. Thus, nanocomposites can significantly reduce the phonon thermal conductivity ( $2.5 \text{ W m}^{-1} \text{ K}^{-1}$  in p-type SiGe nanocomposites vs.  $4.6 \text{ W m}^{-1} \text{ K}^{-1}$  in RTG bulk) without significantly reducing the electrical conductivity, resulting in a higher  $ZT$ .<sup>[19]</sup> In some early reports,  $ZT$  decreases when the grain size is reduced below micrometers<sup>[13]</sup> because of a reduction of electrical conductivity besides the decrease of thermal conductivity. The reason for

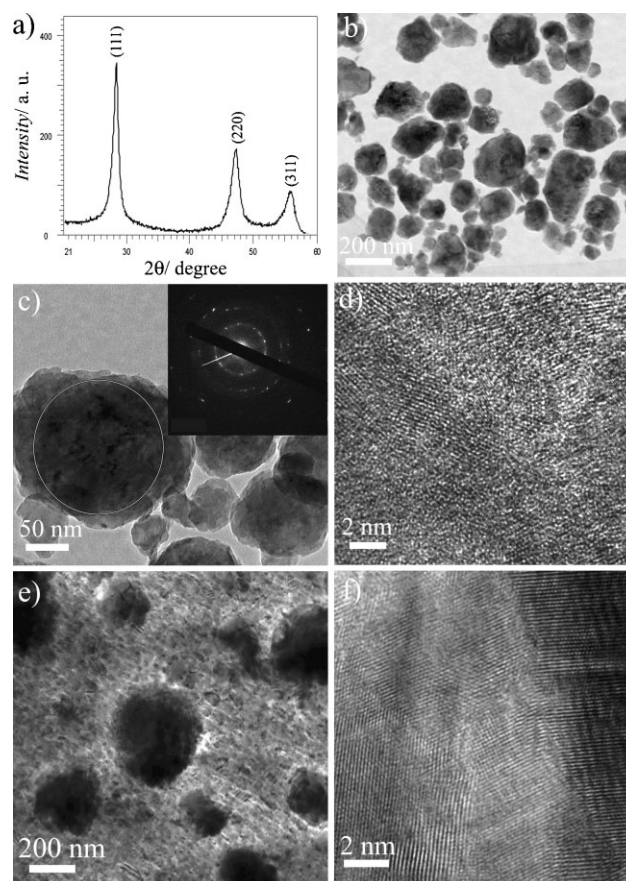


**Figure 7.** a) XRD pattern, b) BF-TEM image at low-magnification, c) BF-TEM image at medium-magnification, and d) HRTEM image of the p-type boron-doped  $\text{Si}_{80}\text{Ge}_{20}$  nanoparticles prepared by ball-milling. e) BF-TEM image and f) HRTEM image of the hot-pressed p-type boron-doped  $\text{Si}_{80}\text{Ge}_{20}$  nanocomposites. The inset in (c) is SAED of an individual nanograin indicating the polycrystalline nature of the nanograin. Reproduced with permission from Ref. [54]. Copyright 2008, American Chemical Society.

electrical conductivity was not clearly stated, but we theorize that it is because of massive defects creation during the ball milling process and some contaminations.

p-type SiGe nanocomposites with high  $ZT$  have been prepared using the same technique as that used for  $\text{Bi}_2\text{Te}_3$  nanocomposites. p-type (boron doped)  $\text{Si}_{80}\text{Ge}_{20}$  single-phase nanoparticles were first prepared by a high-energy ball-mill technique from the individual elements.<sup>[54]</sup> The prepared SiGe nanoparticles are a single-phase boron-doped  $\text{Si}_{80}\text{Ge}_{20}$  alloy (Fig. 7a). The crystallinity of the mechanically alloyed SiGe nanoparticles is different from that of the ball-milled  $\text{Bi}_2\text{Te}_3$  nanoparticles. The mechanical alloyed  $\text{Si}_{80}\text{Ge}_{20}$  nanoparticles are polycrystalline (Fig. 7c and d) consisting of several sub-nanograins (Fig. 7d) while the mechanically alloyed  $\text{Bi}_2\text{Te}_3$  nanoparticles are single crystals (Fig. 4). Similar polycrystalline structure is also observed on ball-milled pure Si nanopowders. X-Ray diffraction (XRD) and TEM images indicate that the agglomerated particles vary in size from 20 nm to 200 nm. The microstructure can be explained by the high-energy ball-milling theory.<sup>[143,144]</sup>

There are many defects inside individual sub-nanograins (Fig. 7d) because the nanograins are formed by a low-temperature mechanical alloying process and not by high-temperature melting and solidification. High stresses are expected in the ball-milled SiGe nanoparticles. Dislocations and atomic level strains are usually produced in ball-milled nanoparticles<sup>[145]</sup> and detailed information can be found in the articles on high-energy ball-milling.<sup>[85,86,145]</sup>

After hot-pressing, the grain size in the p-type Si<sub>80</sub>Ge<sub>20</sub> nanocomposites is about 20–100 nm (Fig. 7e), about two to five times the size of the initial nanopowders, indicating some grain growth during the hot-pressing process. These nanograins are highly crystalline, completely random, closely packed (Fig. 7f), and have clean boundaries, consistent with the measured density (2.88 g cm<sup>-3</sup>, the theoretical density value).

The Seebeck coefficient of the p-type Si<sub>80</sub>Ge<sub>20</sub> nanocomposites is comparable to that of the RTG samples, while the electrical conductivity is higher than that of the RTG samples over the entire temperature range. More importantly, the thermal conductivity of the nanostructured bulk samples is much lower than that of the RTG samples over the whole temperature range up to 1000 °C, which leads to a peak ZT of about 0.95 in the ball-milled and hot-pressed p-type Si<sub>80</sub>Ge<sub>20</sub> nanocomposites (Fig. 8). Such a peak ZT value is about a 90% improvement over that of the p-type RTG SiGe samples (peak ZT = 0.5) presently used in space missions and 50% above that of the reported record value (peak ZT = 0.65).<sup>[28]</sup>

The significant reduction of the thermal conductivity in the nanostructured samples is mainly due to the increased phonon scattering at the numerous interfaces of the nanocomposites. Since the electrical conductivity of the nanocomposites is similar to that of the RTG samples, the actual lattice thermal conductivity is reduced by a factor of two based on the experimental data shown in Figure 8a.

p-type SiGe composites have also been reported by other groups.<sup>[94,98,127,146]</sup> The grain size of these reported composites is in micrometers. Although thermal conductivity is decreased, ZT is decreased because of the decrease of electrical conductivity and Seebeck coefficient.

### 3.2.2. n-type Si<sub>80</sub>Ge<sub>20</sub> Nanocomposites

The microstructure of the mechanically alloyed n-type Si<sub>80</sub>Ge<sub>20</sub> nanoparticles is very similar to that of the mechanically alloyed p-type nanoparticles. Phosphorus-doped Si<sub>80</sub>Ge<sub>20</sub> single-phase nanoparticles are synthesized using ball-milling (Fig. 9a). The particle size of the as-prepared ball-milled nanopowders is in the range of 30–200 nm (Fig. 9b and c). These nanoparticles are composed of many small crystalline sub-nanograins, similar to the p-type mechanically alloyed SiGe nanoparticles. The size of the sub-nanograins is in the range of 5–15 nm (Fig. 9d) with an average size of 12 nm.

After hot-pressing, an average grain size in the hot-pressed Si<sub>80</sub>Ge<sub>20</sub> nanocomposites is 22 nm (Fig. 9e), indicating that the grain size is almost doubled after hot-pressing, but is still very small. These nanometer-sized grains with random crystalline orientations (Fig. 9f) promote phonon scattering much more effectively than the micrometer-sized grains in the bulk RTG SiGe materials. X-Ray diffraction study indicates that the stress of the hot-pressed nanocomposites is much smaller than that of the as-

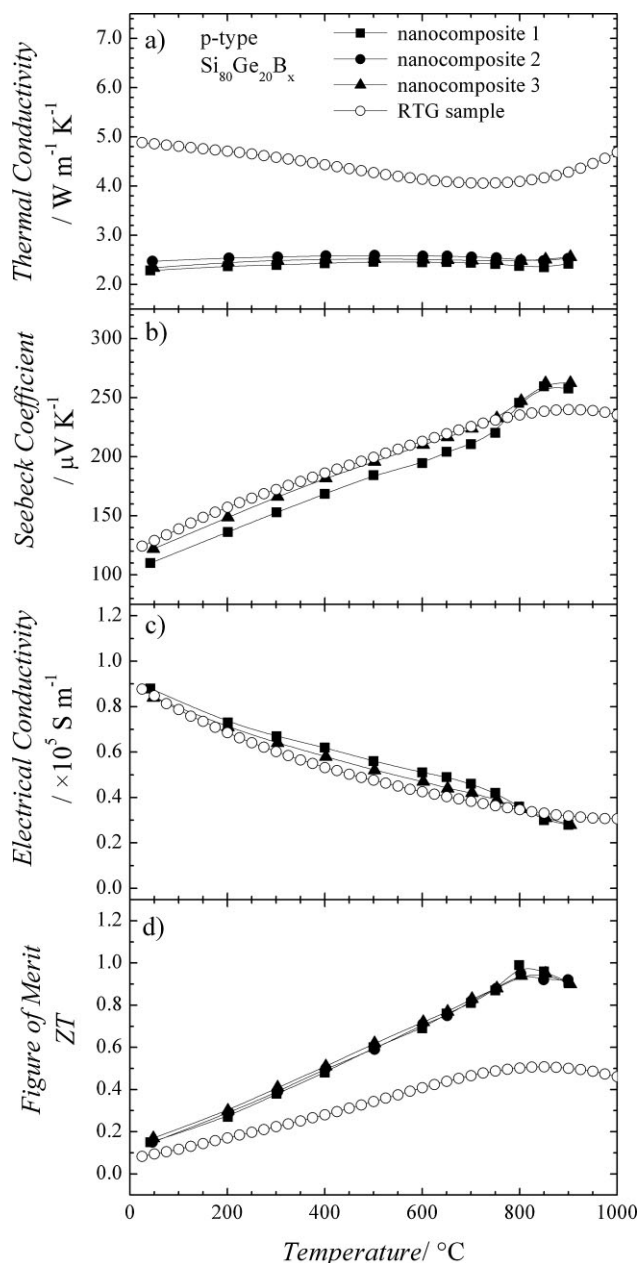


**Figure 8.** Temperature dependence of a) thermal conductivity, b) Seebeck coefficient, c) electrical conductivity, and d) dimensionless ZT of three hot-pressed p-type Si<sub>80</sub>Ge<sub>20</sub> nanocomposites (squares, circles, and triangles), in comparison with p-type SiGe bulk samples used in RTGs for space power missions (open circles). Reproduced with permission from Ref. [54]. Copyright 2008, American Chemical Society.)

prepared ball-milled nanoparticles, with the strain value being ten times lower in the hot-pressed nanocomposites. This smaller strain in the nanocomposites is understandable since the hot-pressing temperature is above 1000 °C, allowing the stresses built up in the nanoparticles during the ball-milling process to be relaxed.

Examining the temperature-dependent thermal conductivity, we can clearly see that the n-type Si<sub>80</sub>Ge<sub>20</sub> nanocomposites have a

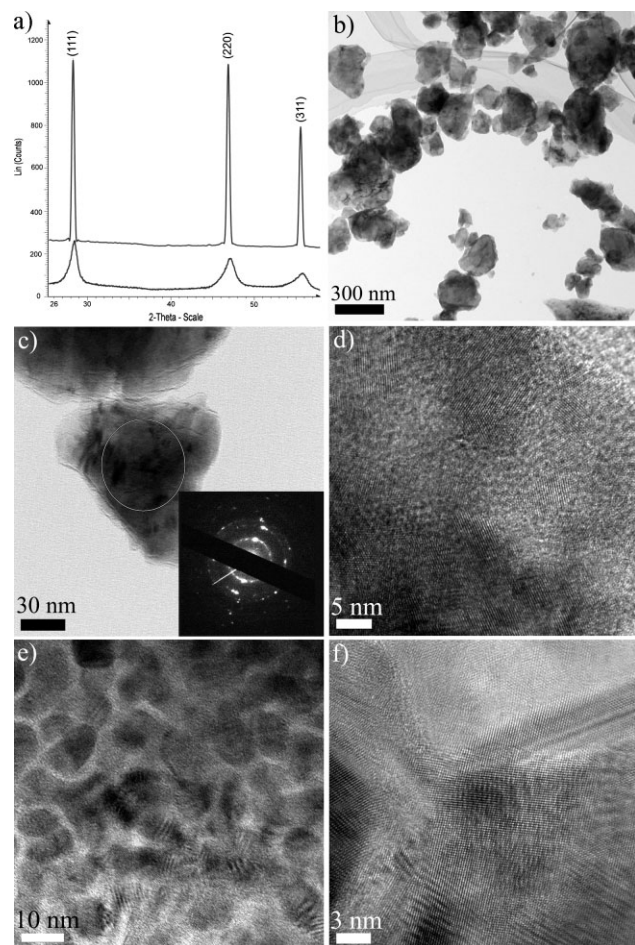


**Figure 9.** a) XRD pattern, b) BF-TEM image at low-magnification, c) BF-TEM image at medium-magnification, and d) HRTEM image of n-type phosphorus-doped  $\text{Bi}_{80}\text{Ge}_{20}$  nanoparticles. e) BF-TEM and f) HRTEM images of hot-pressed n-type  $\text{Si}_{80}\text{Ge}_{20}$  nanocomposites made from the nanoparticles shown in (b). The inset of (c) shows a SAED pattern of an individual nanoparticle. Reproduced with permission from Ref. [56]. Copyright 2008, American Institute of Physics.

much lower thermal conductivity than that of the RTG samples with grain size of 1–10  $\mu\text{m}$  (Fig. 10a). Based on the measured electrical conductivity of the n-type  $\text{Si}_{80}\text{Ge}_{20}$  nanocomposites and RTG samples,  $\kappa_e = 0.77 \text{ W m}^{-1} \text{ K}^{-1}$  at room temperature for RTG samples, whereas  $\kappa_e = 0.55 \text{ W m}^{-1} \text{ K}^{-1}$  at room temperature for a typical nanocomposite. By subtracting the electronic contribution  $\kappa_e$  from the total thermal conductivity  $\kappa$ , the lattice thermal conductivity of the nanocomposite samples is  $\sim 1.8 \text{ W m}^{-1} \text{ K}^{-1}$  at room temperature, which is about 47% of the RTG samples ( $\sim 3.8 \text{ W m}^{-1} \text{ K}^{-1}$ ). The decrease of the lattice thermal conductivity is mainly due to a stronger boundary phonon scattering in the nanostructured samples.

The Seebeck coefficient of the nanocomposite samples is similar to that of the RTG samples at below 400  $^{\circ}\text{C}$  and above 700  $^{\circ}\text{C}$ , and is slightly higher than that of the RTG samples between 400  $^{\circ}\text{C}$  and 700  $^{\circ}\text{C}$  (Fig. 10b). The electrical conductivity of the n-type nanocomposites is normally lower than that of the RTG

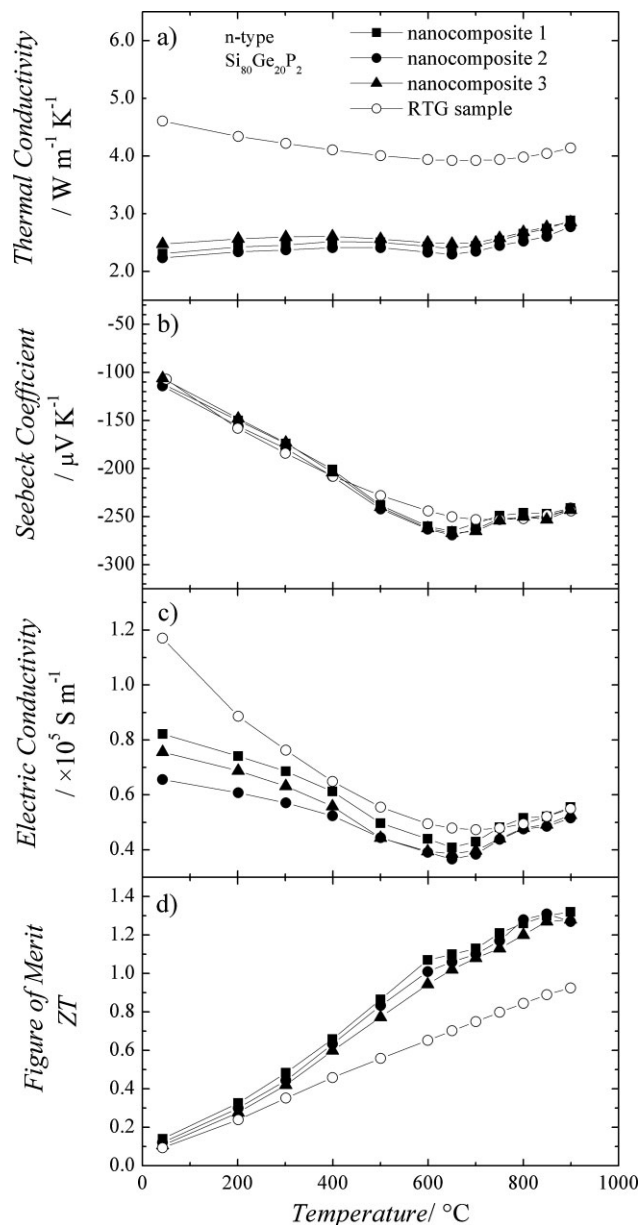


**Figure 10.** Temperature dependence of a) thermal conductivity, b) Seebeck coefficient, c) electrical conductivity, and d) dimensionless  $ZT$  of three hot-pressed n-type  $\text{Si}_{80}\text{Ge}_{20}$  nanocomposites (squares, triangles, and circles), in comparison with the RTG reference sample (open circles). Reproduced with permission from Ref. [56]. Copyright 2008, American Institute of Physics.

samples in the low temperature region, but is similar above 750  $^{\circ}\text{C}$  (Fig. 10c), although the carrier concentrations for both types of samples determined from Hall effect measurement are almost the same at room temperature ( $\sim 2.2 \times 10^{20} \text{ cm}^{-3}$ ), indicating a lower electron mobility in the nanocomposite samples, reasonable considering the large number of grain boundaries.

As a result, for the n-type  $\text{Si}_{80}\text{Ge}_{20}$  nanocomposites, the  $ZT$  value shows a maximum of about 1.3 at 900  $^{\circ}\text{C}$  which is about 40% higher than that of the RTG reference (0.93; Fig. 10d). The



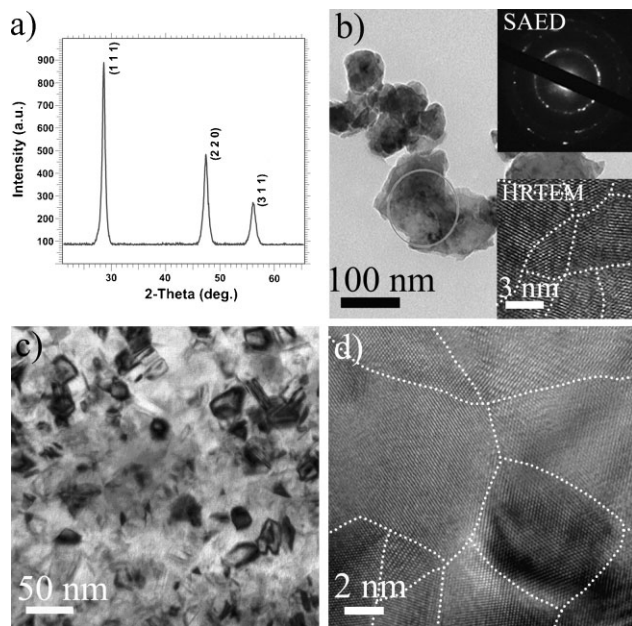


**Figure 11.** a) XRD pattern and b) BF-TEM image of ball-milled  $\text{Si}_{95}\text{Ge}_5$  nanoparticles. c) BF-TEM image and d) HRTEM image of a hot-pressed  $\text{Si}_{95}\text{Ge}_5$  nanocomposite. The insets in (b) are SAED pattern and HRTEM image of the circled region. Reproduced with permission from Ref. [57]. Copyright 2009, American Physical Society.

significant enhancement of  $ZT$  is mainly attributed to the thermal conductivity reduction, which is strongly correlated with the nanostructural features in the n-type  $\text{Si}_{80}\text{Ge}_{20}$  nanocomposites.

### 3.2.3. n-type Si and $\text{Si}_{95}\text{Ge}_5$

$\text{Si}_{95}\text{Ge}_5$  nanoparticles were also synthesized by high-energy ball-milling from Si, Ge, P, and GaP powders. These ball-milled nanoparticles are single phase (Fig. 11a) with a size of 20–150 nm (Fig. 11b). SAED patterns and HRTEM images (insets in Fig. 11b) indicate that the ball-milled nanoparticles also consist of sub-nanograins, similar to what was observed in the heavily doped p-type  $\text{Si}_{80}\text{Ge}_{20}$  nanoparticles (Fig. 7) and n-type  $\text{Si}_{80}\text{Ge}_{20}$  nanoparticles (Fig. 9).

After hot-pressing, most of the nanograins are in the 10–30 nm range (Fig. 11c), larger than the 5–20 nm of the initial nanoparticles due to grain growth during the hot-pressing process. The nanograins are highly crystalline and randomly oriented after hot-pressing (Fig. 11d).

Figure 12 shows the comparative thermoelectric property measurement results for nanostructured Si,  $\text{Si}_{95}\text{Ge}_5$  nanocomposite, bulk Si, and bulk  $\text{Si}_{80}\text{Ge}_{20}$  RTG alloy. Both the nanostructured Si and nanostructured  $\text{Si}_{95}\text{Ge}_5$  samples show a higher electrical conductivity (Fig. 12a) but a lower absolute Seebeck coefficient (Fig. 12b) than that of the bulk  $\text{Si}_{80}\text{Ge}_{20}$  RTG sample. This is mainly attributed to the higher solubility limit of P and the lower alloy scattering of charge carriers in nanostructured Si and nanostructured  $\text{Si}_{95}\text{Ge}_5$  samples in comparison with the bulk  $\text{Si}_{80}\text{Ge}_{20}$  RTG sample. The power factors for both the nanostructured samples (Fig. 12c) are slightly lower than the values calculated for

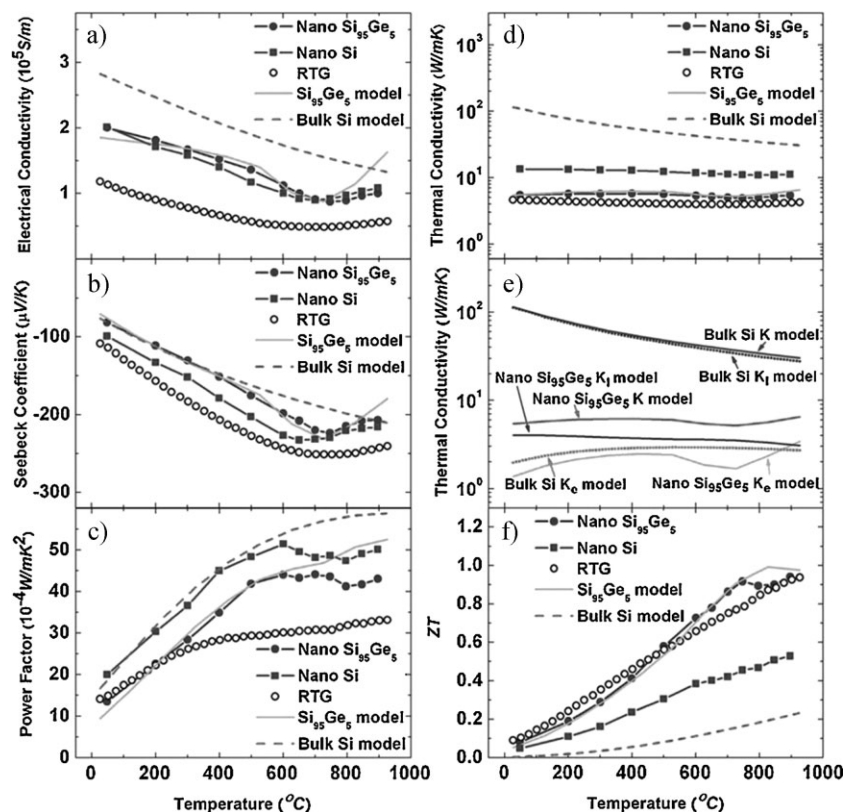
bulk materials with the same carrier-concentration values as measured for the nanostructured samples. The power factor of the nanostructured  $\text{Si}_{95}\text{Ge}_5$  sample is much higher than that of the bulk  $\text{Si}_{80}\text{Ge}_{20}$  RTG sample (Fig. 12c), especially at temperatures above 300 °C. Figure 12d shows the temperature-dependent thermal conductivity of the nanostructured Si and nanostructured  $\text{Si}_{95}\text{Ge}_5$  samples in comparison with bulk Si and bulk  $\text{Si}_{80}\text{Ge}_{20}$  RTG samples. The thermal conductivity of the nanostructured Si shows a significant reduction (by about a factor of 10) compared with that of the heavily doped bulk Si, which is around  $100 \text{ W m}^{-1} \text{ K}^{-1}$ , at room temperature, a clear demonstration of the nanosize effect on phonon scattering. Moreover, with a 5 at% replacement of Si by Ge, the thermal conductivity value of the nanostructured  $\text{Si}_{95}\text{Ge}_5$  is even lower, close to that of the bulk  $\text{Si}_{80}\text{Ge}_{20}$  RTG sample, due to both the nanosize and point defect scattering effects in nanostructured  $\text{Si}_{95}\text{Ge}_5$ . Since the bulk  $\text{Si}_{80}\text{Ge}_{20}$  RTG sample has 20 at% Ge and the  $\text{Si}_{95}\text{Ge}_5$  nanostructure has only 5 at% Ge, a weaker alloy phonon scattering effect is expected in  $\text{Si}_{95}\text{Ge}_5$ . When the Ge concentration is increased from 5 to 20 at%, the thermal conductivity is decreased by another factor of 2 to about  $2\text{--}3 \text{ W m}^{-1} \text{ K}^{-1}$ , but the power factor is also decreased<sup>[56]</sup> accordingly because of the reduced charge mobility due to the alloy scattering of charge carriers.

Figure 12e shows that the calculated thermal conductivity of the  $\text{Si}_{95}\text{Ge}_5$  nanocomposite matches well with the experimental results. The electron contribution to the thermal conductivity is calculated from the electrical conductivity measurement results using the Wiedemann–Franz Law. The Lorenz number is calculated from the bulk model. Our modeling results show that the Lorenz number in bulk SiGe alloy varies from 1.3 to  $2.2 \times 10^{-8} \text{ W } \Omega \text{ K}^{-2}$  from 25 °C to 1000 °C, and that variation within any specific temperature is 0.2 for the range of the doping concentration in our samples. The calculated phonon thermal conductivity is below  $4 \text{ W m}^{-1} \text{ K}^{-1}$  at room temperature and reaches  $3 \text{ W m}^{-1} \text{ K}^{-1}$  at 900 °C (Fig. 12e). The low thermal conductivity for the  $\text{Si}_{95}\text{Ge}_5$  system is mainly attributed to both the enhanced boundary phonon scattering and the alloy effect. Thus, due to the significant thermal conductivity reduction without reduction of the power factor,  $ZT$  of the  $\text{Si}_{95}\text{Ge}_5$  nanocomposites shows a maximum value of 0.95 at 900 °C, which is about the same as that of the bulk n-type  $\text{Si}_{80}\text{Ge}_{20}$  RTG sample (Fig. 12f).

In nanostructured bulk Si, it is reported that the grain boundaries with very high density do not strongly affect electron mobility but dramatically reduce the lattice thermal conductivity.<sup>[100]</sup> The combined transport effects produce an increase in the  $ZT$  of nanostructured bulk Si by a factor of nearly 3.5.

### 3.3. Skutterudite Nanocomposites

Skutterudites have been widely studied for their promising thermoelectric properties,<sup>[147–149]</sup> and are regarded as potential candidates for next-generation thermoelectric materials for electrical power generation using either solar energy or waste heat. Undoped  $\text{CoSb}_3$  is p-type with a  $ZT$  of about 0.2. After doping with rare earth elements,  $ZT$  increases to 0.52 at 600 K for n-type crystals.<sup>[150]</sup> A peak  $ZT$  of 0.7 was achieved in n-type  $(\text{Ni}, \text{Co})_4\text{Sb}_{12}$  nanocomposites produced by the ball-milling and hot-pressing method.<sup>[107]</sup>



**Figure 12.** Temperature-dependent a) electrical conductivity, b) Seebeck coefficient, c) power factor, d) thermal conductivity, e) electron ( $\kappa_e$ ), phonon ( $\kappa_i$ ), and total ( $\kappa$ ) thermal conductivity by modeling, and f) ZT of nanostructured Si (filled squares),  $\text{Si}_{95}\text{Ge}_5$  nanocomposite (filled circles for experiment and solid line for model), bulk Si model (dashed line), and  $\text{Si}_{80}\text{Ge}_{20}$  RTG samples (open circles). Reproduced with permission from Ref. [57]. Copyright 2009, American Physical Society.

Another remarkable feature of skutterudites is that the cage-like open structure of the compounds can be filled with foreign atoms acting as phonon rattlers. The filled foreign atoms scatter phonons strongly and drastically reduce the thermal conductivity of the skutterudite compounds.<sup>[147–149]</sup> With various kinds of atoms filling the cages, an improved ZT can be achieved in  $\text{R}_x\text{Co}_4\text{Sb}_{12}$  ( $\text{R} = \text{Ce},^{[151]} \text{La},^{[152]} \text{Ca},^{[153]} \text{Ba},^{[154]}$  and  $\text{Yb}^{[89,106,155]}$ ). For example, Yb-filled n-type  $\text{Yb}_{0.19}\text{Co}_4\text{Sb}_{12}$  with a peak ZT close to 1 at 373 °C<sup>[106]</sup> and  $\text{Yb}_{0.15}\text{Co}_4\text{Sb}_{12}$  with a peak ZT of about 0.7 at 400 °C<sup>[155]</sup> have been reported. The peak ZT of  $\text{Yb}_x\text{Co}_4\text{Sb}_{12}$  nanocomposites made from the ball-milling and hot-pressing method was increased to 1.2.<sup>[105]</sup>

### 3.3.1. n-type $\text{Yb}_x\text{Co}_4\text{Sb}_{12}$ Nanocomposites

We have tried to obtain  $\text{Yb}_x\text{Co}_4\text{Sb}_{12}$  nanopowders by ball-milling from elements. However, unlike the  $\text{Bi}_2\text{Te}_3$  and  $\text{SiGe}$  systems, only a small portion of the ball-milled nanopowders are mechanically alloyed after high-energy ball-milling, regardless of the ball-milling time. The same phenomenon is also observed in other skutterudites, such as  $\text{CoSb}_3$ ,<sup>[156]</sup>  $(\text{La},\text{Ni},\text{Co})_4\text{Sb}_{12}$ ,<sup>[111]</sup>  $\text{Fe}_x\text{Co}_4\text{Co}_{12-x}$ ,<sup>[91,156]</sup>  $\text{Co}(\text{Sb},\text{Te})_3$ ,<sup>[83]</sup> and  $\text{FeCo}_3\text{Sb}_{12}$ ,<sup>[157]</sup> and in other material systems such as the  $\text{Ag}_{0.8}\text{Pb}_{18+x}\text{SbTe}_{20}$  system.<sup>[81]</sup> This phenomenon is common in mechanical alloying. For some

thermoelectric compounds, such as  $\text{FeSi}_2$ , the ball-milling process does not mechanically alloy Fe and Si elements.<sup>[158]</sup> However, the ball-milling process does mix the elements uniformly at the nanometer scale, facilitating the alloying via chemical reaction during the hot-pressing process.

After the hot-pressing, the nanopowders are completely transformed into a single-phase skutterudite. The average grain size is about 200 to 500 nm (Fig. 13a and b). There are two types of nanograins in the skutterudite nanocomposites: larger ones of about 1  $\mu\text{m}$  in a bar shape (in the middle of Fig. 13a), and smaller ones of about 200–500 nm in a spherical shape. The larger ones could grow from the mechanically alloyed small particles while the smaller ones could form from unalloyed powders.<sup>[107]</sup> Both types of nanograins are well crystallized with clear facets. The crystallized grains are closely packed, implying a high density, consistent with the theoretical density ( $7.6 \text{ g cm}^{-3}$ ).

All the nanograins in the nanocomposites are well crystallized, and the large-angle grain boundaries are clean (Fig. 13b). The excellent crystallinity and clean grain boundaries are needed to achieve good electrical transport properties, whereas the large angle grain boundaries also benefit phonon scattering.

A series of  $\text{Yb}_x\text{Co}_4\text{Sb}_{12}$  ( $x = 0.3, 0.35, 0.4, 0.5$ , and  $1.0$ ) nanostructured samples have also been prepared by ball-milling and hot-pressing.  $\text{Yb}_{0.35}\text{Co}_4\text{Sb}_{12}$  has an optimized lowest thermal conductivity with a minimum of  $2.7 \text{ W m}^{-1} \text{ K}^{-1}$  (Fig. 13c), which leads to the highest observed ZT value among all the samples.<sup>[105]</sup> Below we focus on the  $\text{Yb}_{0.35}\text{Co}_4\text{Sb}_{12}$  nanostructured sample.

The thermoelectric properties of  $\text{Yb}_{0.35}\text{Co}_4\text{Sb}_{12}$  are compared with other reported properties of nanocomposites prepared by the ball-milling and hot-pressing method. The nanocomposites produced here show a much higher electrical conductivity than those reported,<sup>[89,106]</sup> presumably due to the large electron doping effect from the high Yb concentration. The thermal conductivity of the nanocomposites ( $2.7\text{--}3.3 \text{ W m}^{-1} \text{ K}^{-1}$  from room temperature to 600 °C) is almost the same as the thermal conductivity of those prepared by spark plasma sintering ( $2.4\text{--}3.9 \text{ W m}^{-1} \text{ K}^{-1}$ ). The low thermal conductivity of these n-type  $\text{Yb}_x\text{Co}_4\text{Sb}_{12}$  nanocomposites should come from the stronger phonon scattering resulting from the presence of a large concentration of rattlers and an increased concentration of grain boundaries in the nanocomposites. Therefore, the nanocomposites have a higher ZT value than the doped  $\text{Co}_4\text{Sb}_{12}$  reference samples without rattlers ( $ZT = 0.52$  at 600 K<sup>[150]</sup>) as a result of the enhanced power factor and reduced thermal conductivity of the nanocomposites.

ZT increases with temperature and reaches a maximum ( $\sim 1.2$ ) at around 550 °C (Fig. 13f). Similar enhancements have recently been reported by various groups in n-type skutterudite nanocomposites.<sup>[89,106,107,155,159]</sup>

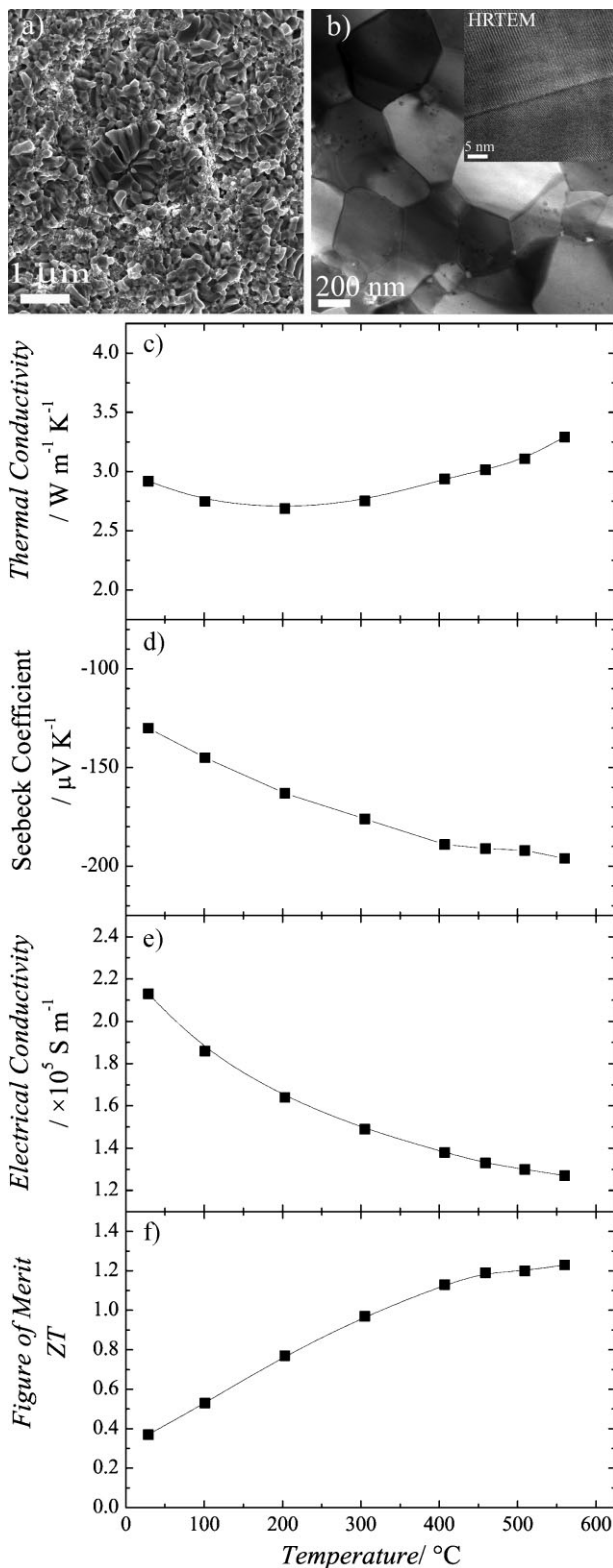


**Figure 13.** a) SEM image, b) BF-TEM image, c) thermal conductivity, d) Seebeck coefficient, e) electrical conductivity, and f) ZT of hot-pressed n-type skutterudite  $\text{Yb}_{0.35}\text{Co}_4\text{Sb}_{12}$  nanocomposites. Inset in (b) is an HRTEM image of a grain boundary. Reproduced with permission from Ref. [105]. Copyright 2009, American Physical Society.

n-type skutterudite  $\text{CoSb}_3$  nanocomposites have also been prepared by other groups using the ball-milling and hot-pressing method.<sup>[109,111,135]</sup>  $ZT < 1.0$  in these nanocomposites because of low electrical conductivity.  $ZT = 1.1$  can be achieved in n-type  $\text{Ba}_{0.24}\text{Co}_4\text{Sb}_{12}$  nanocomposites prepared by ball-milling, followed by cold-pressing and sintering;<sup>[154]</sup>  $ZT = 1.3$  in  $\text{Yb}_x\text{Co}_4\text{Sb}_{12+y}$  nanocomposites by spark plasma sintering method;<sup>[89,160]</sup>  $ZT = 1.1$  in  $\text{CoSb}_{3-x}\text{Te}_x$  nanocomposites by ball-milling and spark plasma sintering method.<sup>[83]</sup>

### 3.3.2. p-type $(\text{La,Ce,Nd})\text{Fe}_{4-x}\text{Co}_x\text{Sb}_{12}$ Nanocomposites

Rare-earth filled and Fe-substituted skutterudites are p-type. Many p-type skutterudite nanocomposites can be prepared using the ball-milling and hot-pressing method.<sup>[112,113,147,157,161–163]</sup> The ball-milled nanoparticles are mixture of Sb, skutterudites, and  $(\text{Co,Fe})\text{Sb}_2$  compounds. After hot-pressing, nanocomposites with a single phase are obtained. The thermal conductivity decreases significantly because of the rattling effect from rare-earth atoms in the voids and the substitution of Fe for Co. The lattice thermal conductivity decreases with the rare-earth filling content. The thermal conductivity can be reduced down to  $4 \text{ W m}^{-1} \text{K}^{-1}$  at room temperature (one third of that of  $\text{CeSb}_3$  samples).<sup>[150]</sup>

$\text{La}_x(\text{Ni,Co})_4\text{Sb}_{12}$  nanocomposites can also be produced by ball-milling and spark plasma sintering. The produced nanocomposites exhibit a lower thermal conductivity than the bulk material.<sup>[111]</sup> Other skutterudite nanocomposites have also been reported, such as  $\text{Sn}_y\text{Fe}_3\text{Co}_5\text{Sb}_{24}$  nanocomposites,<sup>[110]</sup> rare-earth filled  $\text{Fe}_4\text{Sb}_{12}$  skutterudite nanocomposites,<sup>[112]</sup> and  $\text{FeCo}_3\text{Sb}_{12}$  nano-composites.<sup>[113,157]</sup>

### 3.4. PbTe Nanocomposites

Lead telluride (PbTe) is one of the best thermoelectric materials at intermediate temperatures (450–800 K). The peak ZT of PbTe is 0.7 at 700 K. Recently, ZT was doubled to about 1.5 at 773 K in thallium-doped PbTe through an enhancement of the Seebeck coefficient.<sup>[63]</sup> Using thallium-doped PbTe, PbTe nanocomposites with high ZT have also been achieved.

The PbTe nanoparticles are prepared by ball-milling thallium, lead, and tellurium.<sup>[63b]</sup> The microstructure of the ball-milled nanoparticles (Fig. 14a) is similar to that of SiGe alloys. During hot-pressing, the nanoparticles grow quickly, and the grain size in the hot pressed PbTe is bigger than 1  $\mu\text{m}$  (Fig. 14b). Compared with the properties of the ingots, the thermal conductivity of the hot-pressed samples is slightly decreased over the entire temperature range (Fig. 14c) while the electrical conductivity is increased (Fig. 14e). The Seebeck coefficient is slightly decreased at higher temperatures (Fig. 14d). The ZT is the same as the reported values (Fig. 14f).<sup>[63]</sup>

A smaller grain size can lead to further thermal conductivity reduction and a higher ZT. More work is being carried out to decrease the grain size while preserving the electrical conductivity and the Seebeck coefficient.

PbTe nanocomposites with 95% theoretical density are also prepared by the spark plasma sintering method from 100–150 nm nanoparticles.<sup>[73]</sup> The reported ZT of the nanocomposites is 0.1 at room temperature.



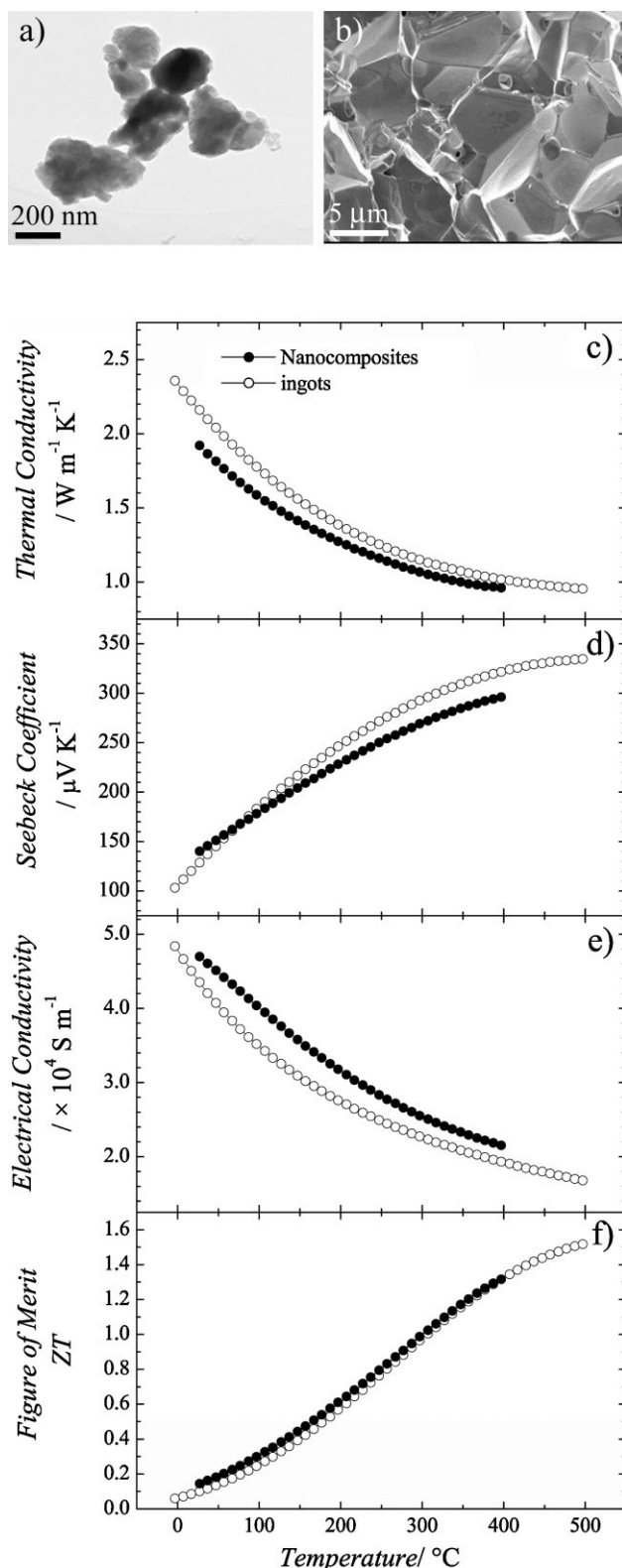


**Figure 14.** a) TEM image of ball-milled PbTe nanopowder. b) SEM image of hot-pressed PbTe nanocomposites. Temperature dependent c) thermal conductivity, d) Seebeck coefficient, e) electrical conductivity, and f) ZT of hot-pressed PbTe nanocomposites. The data of PbTe bulk [63] are also plotted for comparison.

### 3.5. Other Nanocomposites

The ball-milling and hot-pressing method has been widely applied to produce thermoelectric nanocomposites. Besides the above reviewed materials (n-type and p-type  $\text{Bi}_2\text{Te}_3$  nanocomposites, n-type and p-type  $\text{SiGe}$  nanocomposites, n-type and p-type skutterudite  $\text{Co}_4\text{Sb}_{12}$  nanocomposites, p-type  $\text{PbTe}$  nanocomposites), the technique has also been applied to other material systems, such as  $\text{Mg}_2\text{Si}$ . Table 1 lists some typical nanocomposites produced by the ball-milling and hot-pressing method. The thermal conductivity of these nanocomposites is lower than that of the single-crystalline bulk materials. In some nanocomposites prepared by the ball-milling and hot-pressing method, the power factor is also enhanced. It is reported that the power factor of n-type  $\text{Bi}_{85}\text{Sb}_{14}\text{Ag}$  nanocomposites is  $2.98 \times 10^{-3} \text{ W m}^{-1} \text{ K}^{-2}$  at 255 K,<sup>[164]</sup> which is about three times that of  $\text{Bi}_{85}\text{Sb}_{15}$  single crystals. The power factor of a  $\text{Bi}_{85}\text{Sb}_{13}\text{Pr}_2$  nanocomposites is  $3.8 \times 10^{-3} \text{ W m}^{-1} \text{ K}^{-2}$  at 235 K,<sup>[165]</sup> which is about four times that of  $\text{Bi}_{85}\text{Sb}_{15}$  single crystals.

Besides the ball-milling and hot-pressing method, thermoelectric nanocomposites are also prepared by other methods. For example,  $\text{Ga}_m\text{Sb}_n\text{Te}_{1.5+m+n}$  nanocomposites with peak  $ZT = 0.98$  can be prepared by the spark plasma sintering method from ball-milled nanoparticles.<sup>[120]</sup> The nanograin size is small (less than 30 nm).  $\text{Zn}_4\text{Sb}_3$  nanocomposites can be produced by sintering cold-pressed samples.<sup>[92]</sup> The thermal conductivity of  $\text{Ag}_{0.8}\text{Pb}_{18+x}\text{SbTe}_{20}$  nanocomposites decreases 40% after ball-milling and spark plasma sintering and a peak  $ZT$  of 1.3 has been reported at 300 °C.<sup>[81]</sup> In  $\text{Bi}_{100-x}\text{Sb}_x$  nanocomposites obtained by ball-milling and extrusion method, the thermal conductivity decreases 75%.<sup>[75]</sup> These nanocomposites are also listed in Table 1.

In all of these thermoelectric nanocomposites, the thermal conductivity is decreased. Despite this,  $ZT$  is not necessarily enhanced, and could even be decreased, depending on the change of electrical conductivity and Seebeck coefficient.

To further decrease the thermal conductivity, additional phases have been dispersed into the nanocomposites. It is postulated that the addition of second-phase nanoparticles will work as phonon scattering centers and further decrease thermal conductivity.  $\text{ZnO}_2$  and rare-earth oxides have been added into  $\beta\text{-FeSi}_2$  nanocomposites.<sup>[121]</sup> It is reported that the dispersion of  $\text{Y}_2\text{O}_3$  nanoparticles doubles the  $ZT$  of n-type  $\beta\text{-FeSi}_2$  nanocomposites from 0.35 to 0.63 when 2 wt%  $\text{Y}_2\text{O}_3$  is added.<sup>[122]</sup> The thermal conductivity decreases to 0.7 from  $4.5 \text{ W m}^{-1} \text{ K}^{-1}$ .

$\text{TiB}_2$  can be dispersed into  $\beta\text{-FeSi}_2$  nanocomposite using the ball-milling and hot-pressing method.<sup>[114]</sup> However, increasing  $\text{TiB}_2$  content (0–30 vol%) results in a decreased power factor and  $ZT$ .  $\text{TiB}_2$  has also been dispersed into  $\text{B}_4\text{C}$  nanocomposites using the ball-milling and hot-pressing method.<sup>[126,166]</sup>  $\text{B}_4\text{C}$  works as a thermoelectric host. Both the thermal conductivity and the electrical conductivity decrease with  $\text{TiB}_2$  content from 0 to 25 vol% and  $ZT$  also decreases.

$\text{BN}$  and  $\text{WO}_3$  can be dispersed into p-type  $(\text{Bi,Sb})_2\text{Te}_3$  nanocomposites using the ball-milling and hot-pressing method.<sup>[124]</sup> The thermal conductivity decreases slightly from  $1.5 \text{ W m}^{-1} \text{ K}^{-1}$  to  $1.2 \text{ W m}^{-1} \text{ K}^{-1}$  when the volume fraction of  $\text{BN}$  and  $\text{WO}_3$  is increased from 0 vol% to 7 vol%.  $ZT$  decreases with  $\text{BN}$  and  $\text{WO}_3$  content because of a rapid decrease of the electrical conductivity.

In all of these nanocomposites with additions, the thermal conductivity indeed decreases with increasing volume fraction of the second phase because of the enhanced phonon scattering. However, the addition of the second phase also decreases the electrical conductivity and Seebeck coefficient.  $ZT$  usually decreases because of a greater reduction in electrical conductivity and Seebeck coefficient. In order to increase  $ZT$  of the nanocomposites with addition, it is necessary to avoid the decrease of electrical conductivity and Seebeck coefficient after the addition of a second phase.

It is also suggested that amorphous structure and lattice distortion in the thermoelectric materials can contribute to the decrease in thermal conductivity<sup>[120]</sup> as well as atomic disorder does.<sup>[167]</sup> This is another approach to increase  $ZT$  through introducing amorphous or defect phonon scattering centers. Further investigation into this method is expected.

#### 4. Phonon Transport in Nanocomposites

Since most nanocomposites to date have achieved their high  $ZT$  values by a reduction in lattice thermal conductivity, one might expect that phonon transport in nanocomposites is fairly well understood. However, the situation turns out to be just the opposite. Even in bulk materials, there is much uncertainty regarding the values of key quantities such as the phonon mean free path. Furthermore, the precise way in which interfaces affect phonon transport to reduce thermal conductivity in nanocomposites remains poorly understood. Theoretical predictions for the lower limit of thermal conductivity in nanostructured materials also turn out to be wrong, as was experimentally demonstrated by Cahill.<sup>[168]</sup> This physical understanding is crucial to further reducing the thermal conductivity, however, and so here we highlight what is known about phonon transport and what we seek to understand.

Nanocomposites have shown that they are able to achieve a thermal conductivity lower than that of their bulk counterparts. Before the creation of nanostructured materials it was believed that the lower limit to the thermal conductivity was set by the value obtained by an alloy, as in SiGe, and this lower value of the thermal conductivity was termed the “alloy limit.” While this “limit” remained for fifty years, recently nanocomposites have exhibited a lower thermal conductivity than that of their corresponding alloy.<sup>[54,56]</sup>

The reason why this is possible is now fairly well understood. Phonons in a material have a spectrum of wavelengths and mean free paths, each of which contributes to the total thermal conductivity. Introducing impurity atoms to make an alloy causes phonons to be scattered by impurity atoms, which are only effective in scattering short wavelength, high frequency phonons. This scattering process is very similar to Rayleigh scattering, where high frequency light (short wavelength blue light) is scattered preferentially by atmospheric molecules. Thus while high frequency phonons are strongly scattered in alloys, mid-to-long-wavelength phonons are still able to transport heat. Furthermore, it has been shown previously that in bulk Si these mid-to-long-wavelength modes can actually carry a substantial fraction of the heat.<sup>[169]</sup> By incorporating structures with a larger characteristic length than that of an impurity atom, an interface scattering

mechanism is introduced which scatters mid-to long-wavelength phonons, resulting in a further reduced thermal conductivity that is lower than the alloy limit. This scattering mechanism is most effective when the structures are smaller than the phonon mean free path, which is approximately one hundred nanometers in SiGe.

This physical picture gives a good qualitative understanding of why nanocomposites are able to beat the alloy limit. Simple phonon models based on the Callaway model of thermal conductivity,<sup>[170,171]</sup> which uses the Debye model, along with an additional interface scattering term have been able to explain thermal conductivity data for  $\text{In}_{0.53}\text{Ga}_{0.47}\text{As}/\text{ErAs}$  nanostructures<sup>[42]</sup> and Si nanowires.<sup>[43]</sup> However, while these models can fit the data by adjusting various fitting parameters, a more careful examination shows that many of the model's fundamental predictions are not correct. Figure 15a and b show the cumulative distribution function of thermal conductivity with respect to phonon wavelength and mean free path for the Callaway model

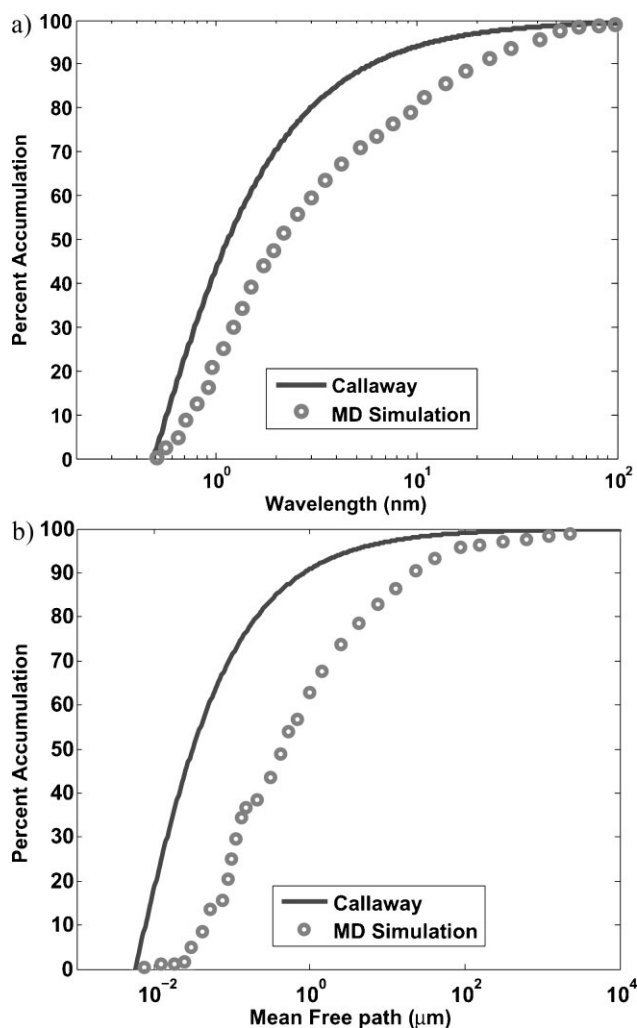


**Figure 15.** Cumulative distribution function of lattice thermal conductivity with respect to a) phonon wavelength and b) phonon mean free path predicted by the Callaway model and molecular dynamics simulations [169] in bulk, undoped Si at 300 K.

and a more exact molecular dynamics simulation<sup>[169]</sup> in bulk, undoped Si at 300 K. From here we see that while the simple Callaway model can be adjusted to give the correct total thermal conductivity, the more quantitative results, such as phonon mean free path and wavelength, are not consistent even for the bulk case; in this case the spectral dependence of the thermal conductivity has only fair agreement with the molecular dynamics result, while the mean free path accumulation does not agree well. Crucially, the key result that long mean free path phonons carry a large fraction of the heat in undoped Si, which is an important fact to know when designing thermoelectric materials, is not predicted by the Callaway model. Thus even phonon transport in bulk materials is not well understood, and new discoveries are still taking place; Morelli et. al. recently reported an unusually low thermal conductivity in bulk cubic AgSbTe<sub>2</sub> due to extremely anharmonic bonds.<sup>[172]</sup>

Nanostructures add another layer of complexity to this problem because they contain many interfaces with spacing smaller than the phonon mean free path, which introduces a thermal boundary resistance between different regions of the nanocomposite. While researchers have been able to use thermal boundary resistance to obtain a low thermal conductivity, there is currently limited ability to predict the thermal boundary resistance despite many years of research.<sup>[173,174]</sup> Thermal boundary resistance has also been identified as the key mechanism for the low thermal conductivity in superlattices, rather than the periodicity of the superlattices.<sup>[36,175,176]</sup> Such understanding led to the concept of a nanocomposite. Efforts have been made to calculate thermal boundary resistance using the Boltzmann equation<sup>[177]</sup> and Monte Carlo simulations,<sup>[178]</sup> and Minnich and Chen introduced a modified theory to analytically compute the thermal conductivity of nanocomposites.<sup>[179]</sup> Similarly, Peierls instability can also lead to low thermal conductivity and *ZT* enhancement.<sup>[21]</sup>

However, existing models cannot give an accurate prediction for the phonon transmission at a single interface, a fundamental parameter in predicting thermal boundary resistance. Nanoparticles inside the composites have multiple interfaces, raising questions about phonon scattering by these particles. In the past, scattering models based on Rayleigh scattering<sup>[42]</sup> and acoustic Mie scattering theory<sup>[180]</sup> have been used to treat nanoparticle scattering. These models, however, do not include interfacial roughness effects and the effects of scattering inside the particle. Although molecular dynamics<sup>[181]</sup> may be a potential tool, available computation power at this stage limits the size of the nanoparticles that can be treated.

As discussed in the introduction to this section, this lack of understanding affects our ability to design and optimize nanostructured materials to have low thermal conductivity. For example, we are currently unable to answer questions such as which phonon modes are the dominant heat carriers in nanocomposites, what is the optimal size distribution of nanostructures, what type of interface leads to the strongest phonon scattering, or what is the interfacial resistance and reflectivity of a nanocomposite interface. In fact, it is not even clear what is the lower limit to the thermal conductivity in a nanostructure. For bulk materials, the criterion that the phonon mean free path must be at least half the phonon wavelength<sup>[182,183]</sup> sets the lower limit. This might not be the case in nanostructured materials, however. Chen has suggested that the minimum

thermal conductivity in nanostructures is likely lower than in bulk materials because the minimum thermal conductivity theory for bulk materials is based on isotropic scattering, while in nanostructures, interfacial scattering is highly anisotropic.<sup>[34a]</sup> Cahill has experimentally demonstrated that the thermal conductivity of layered WSe<sub>2</sub> is six times lower than the value predicted by theory and only twice that of air, an experimental verification that nanostructures can affect phonon transport in ways that are not accounted for by current theories.<sup>[168,184]</sup>

It is clear there are many unanswered questions in phonon transport that critically affect how we design nanostructured materials to exhibit reduced thermal conductivity. Gaining a better understanding of the fundamentals of phonon transport in nanostructured materials is thus a key challenge. There is much work to be done, but it is expected that with a better understanding of phonon transport, further lattice thermal conductivity reductions in nanocomposite systems should be possible.

## 5. Conclusions and Outlook

Thermoelectric nanocomposites with high *ZT* have been successfully produced using a nanostructuring approach. The nanocomposites consist of nanograins with structural defects. The unique nanostructures of the nanocomposites reduce the thermal conductivity by increasing phonon scattering from the high density of imperfections in the nanocomposites. Simultaneously, the high electrical conductivity and power factor of the nanocomposites are preserved while the phonon thermal conductivity is significantly reduced, resulting in a high *ZT*. In some cases, electrical conductivity and Seebeck coefficient are increased slightly while the thermal conductivity is decreased, greatly enhancing *ZT*. High *ZT* has been achieved in many thermoelectric nanocomposites. For example, peak *ZT* is increased to 1.4 in p-type Bi<sub>2</sub>Sb<sub>2-x</sub>Te<sub>3</sub> nanocomposites from 1.0 in bulk, to 0.95 in p-type Si<sub>80</sub>Ge<sub>20</sub> nanocomposites from 0.65 in bulk, and to 1.3 in n-type Si<sub>80</sub>Ge<sub>20</sub> nanocomposites from 0.9 in bulk. These nanocomposites with enhanced *ZT* have significant commercial potential for industrial waste heat recovery, space power generation, and solar power conversion applications.

More investigation is needed to further enhance *ZT*. In the present nanocomposites, the grain size is usually several tens to one hundred nanometers, relatively large in comparison with the phonon mean free path. This is why it is expected that it is still possible to reduce the thermal conductivity of the nanocomposites. Nanocomposites with smaller grain size are expected by limiting the grain growth during the densification process in the nanostructuring approach. The smaller grain size will hopefully reduce thermal conductivity to 1 W m<sup>-1</sup> K<sup>-1</sup> or less, further enhancing *ZT*. In order to decrease the thermal conductivity to 1 W m<sup>-1</sup> K<sup>-1</sup>, phonon transport in the nanocomposites needs to be understood in greater detail.

It is reported that the power factor is increased in some nanocomposites. However, the thermal conductivity in these nanocomposites is still high, which gives us hope to further improve *ZT* if the thermal conductivity can be reduced significantly. In the coming years, it is important to determine effective strategies to simultaneously improve the power factor and reduce the thermal conductivity.



A ZT of 2 can be achieved in these nanocomposites if the thermal conductivity is reduced to below  $1 \text{ W m}^{-1} \text{ K}^{-1}$  and the power factor is further improved. The thermoelectric devices fabricated from these high ZT nanocomposites are expected to find widespread use in applications such as refrigeration, air-conditioning, and high power commercial generators. In the not too distant future, thermoelectric devices could contribute to a renewable energy supply in the global marketplace, ensuring a future source of clean, reliable energy and protecting our planet's environment.

## Acknowledgements

The authors are thankful to Bed Poudel, Yi Ma, Xiao Yan, Giri Joshi, Xiaowei Wang, Gaohua Zhu, Jian Yang, and Bo Yu for their respective valuable experimental contributions. Sincere thanks are due to Professor M. S. Dresselhaus for fruitful cooperation. This work has been funded by DOE DE-FG02-00ER45805 (ZFR), NSF NIRT 0506830 (GC and ZFR), DOE DE-FG02-08ER46516 (GC and ZFR), and DOE DE-SC0001299 (GC and ZFR).

Received: August 12, 2009

Published online: December 15, 2009

- [1] H. J. Goldsmid, *Thermoelectric Refrigeration*, Plenum Press, New York **1964**.
- [2] D. D. Pollock, *Thermocouples: Theory and Properties*, CRC Press, Boca Raton, FL **1991**.
- [3] *CRC Handbook of Thermoelectrics* (Ed.: D. M. Rowe), CRC Press, Boca Raton, FL **1995**.
- [4] *Recent Trends in Thermoelectric Materials Research III*, Vol. 71 (Ed.: T. M. Tritt), Academic Press, San Diego, CA **2001**.
- [5] *Thermoelectrics Handbook: Macro to Nano* (Ed.: D. W. Rowe), CRC/Taylor & Francis, Boca Raton, FL **2006**.
- [6] C. Wood, *Rep. Prog. Phys.* **1988**, 51, 459.
- [7] F. J. DiSalvo, *Science* **1999**, 285, 703.
- [8] B. C. Sales, *Science* **2002**, 295, 1248.
- [9] S. B. Riffat, X. Ma, *Appl. Therm. Eng.* **2003**, 23, 913.
- [10] L. E. Bell, *Science* **2008**, 321, 1457.
- [11] G. J. Snyder, E. S. Toberer, *Nat. Mater.* **2008**, 7, 105.
- [12] A. F. Ioffe, *Physics of Semiconductors*, Academic Press, New York **1960**.
- [13] C. B. Vining, *J. Appl. Phys.* **1991**, 69, 331.
- [14] J. Yang, T. Caillat, *MRS Bulletin* **2006**, 31, 224.
- [15] D. Y. Chung, T. Hogan, P. Brazis, M. Rocci-Lane, C. Kannewurf, M. Bastea, C. Uher, M. G. Kanatzidis, *Science* **2000**, 287, 1024.
- [16] B. Wölfling, C. Kloc, J. Teubner, E. Bucher, *Phys. Rev. Lett.* **2001**, 86, 4350.
- [17] a) V. L. Kuznetsov, L. A. Kuznetsova, A. E. Kaliazin, D. M. Rowe, *J. Appl. Phys.* **2000**, 87, 7871. b) J. L. Cohn, G. S. Nolas, V. Fessatidis, T. H. Metcalf, G. A. Slack, *Phys. Rev. Lett.* **1999**, 82, 779. c) X. F. Tang, P. Li, S. K. Deng, Q. J. Zhang, *J. Appl. Phys.* **2008**, 104, 013706. d) S. K. Deng, X. F. Tang, P. Li, Q. J. Zhang, *J. Appl. Phys.* **2008**, 103, 073503.
- [18] J. Androulakis, C. H. Lin, H. J. Kong, C. Uher, C. Wu, T. Hogan, B. A. Cook, T. Caillat, K. M. Paraskevopoulos, M. Kanatzidis, *J. Am. Chem. Soc.* **2007**, 129, 9780.
- [19] a) K. F. Hsu, S. Loo, F. Guo, W. Chen, J. S. Dyck, C. Uher, T. Hogan, E. K. Polychroniadis, M. G. Kanatzidis, *Science* **2004**, 303, 818. b) J. Androulakis, K. F. Hsu, R. Pcionek, H. Kong, C. Uher, J. J. D'Angelo, A. Downey, T. Hogan, M. G. Kanatzidis, *Adv. Mater.* **2006**, 18, 1170. c) P. F. P. Poudeu, J. D'Angelo, A. D. Downey, J. L. Short, T. P. Hogan, M. G. Kanatzidis, *Angew. Chem. Int. Ed.* **2006**, 45, 3835. d) A. Guéguen, P. F. P. Poudeu, C. P. Li, S. Moses, C. Uher, J. He, V. Dravid, K. M. Paraskevopoulos, M. G. Kanatzidis, *Chem. Mater.* **2009**, 21, 1683.
- [20] G. S. Nolas, J. Poon, M. Kanatzidis, *MRS Bull.* **2006**, 31, 199.
- [21] J. S. Rhyee, K. H. Lee, S. M. Lee, E. Cho, S. I. Kim, E. Lee, Y. S. Kwon, J. H. Shim, G. Kotliar, *Nature* **2009**, 459, 965.
- [22] G. S. Nolas, J. Sharp, H. J. Goldsmid, *Thermoelectrics: Basic Principles and New Materials Developments*, Springer, New York **2001**.
- [23] *Chemistry, Physics, and Materials Science of Thermoelectric Materials: Beyond Bismuth Telluride* (Eds: M. G. Kanatzidis, S. D. Mahanti, T. P. Hogan), Kluwer Academic/Plenum Publishers, New York **2003**.
- [24] K. Koumoto, I. Terasaki, R. Funahashi, *MRS Bull.* **2006**, 31, 206.
- [25] N. Savvides, H. J. Goldsmid, *J. Phys. C: Solid State Phys.* **1980**, 13, 4657.
- [26] N. Savvides, H. J. Goldsmid, *J. Phys. C: Solid State Phys.* **1980**, 13, 4671.
- [27] D. M. Rowe, V. S. Shukla, N. Savvides, *Nature* **1981**, 290, 765.
- [28] C. B. Vining, W. Laskow, J. O. Hanson, R. R. V. der Beck, P. D. Gorsuch, *J. Appl. Phys.* **1991**, 69, 4333.
- [29] D. M. Rowe, L. W. Fu, S. G. K. Williams, *J. Appl. Phys.* **1993**, 73, 4683.
- [30] A. A. Joraid, *J. Mater. Sci.* **1995**, 30, 744.
- [31] C. W. Nan, R. Birringer, *Phys. Rev. B* **1998**, 57, 8264.
- [32] D. B. Hyun, J. S. Hwang, J. D. Shim, *J. Mater. Sci.* **2001**, 36, 1285.
- [33] D. H. Kim, T. Mitani, *J. Alloy. Compd.* **2005**, 399, 14.
- [34] a) G. Chen, in *Recent Trends in Thermoelectric Materials Research III*, Vol. 71 (Ed.: T. Tritt), Academic Press, San Diego, CA **2001**, pp. 203–259. b) G. Chen, M. S. Dresselhaus, J.-P. Fleurial, T. Caillat, *Int. Mat. Rev.* **2003**, 48, 45. c) G. Chen, A. Shakouri, *J. Heat Transfer* **2002**, 124, 242.
- [35] L. D. Hicks, *Phys. Rev. B* **1993**, 47, 16631.
- [36] a) G. Chen, *Phys. Rev. B* **1998**, 57, 14958. b) H. Q. Liu, Y. Song, S. N. Zhang, X. B. Zhao, F. P. Wang, *J. Phys. Chem. Solids* **2009**, 70, 600.
- [37] R. Yang, G. Chen, *Phys. Rev. B* **2004**, 69, 195316.
- [38] M. S. Dresselhaus, G. Chen, M. Y. Tang, R. G. Yang, H. Lee, D. Z. Wang, Z. F. Ren, J. P. Fleurial, P. Gogna, *Adv. Mater.* **2007**, 19, 1043.
- [39] a) T. Koga, S. B. Cronin, M. S. Dresselhaus, J. L. Liu, K. L. Wang, *Appl. Phys. Lett.* **2000**, 77, 1490. b) X. B. Zhao, S. H. Yang, Y. Q. Cao, J. L. Mi, Q. Zhang, T. J. Zhu, *J. Electron. Mater.* **2009**, 38, 1017. c) Q. Zhang, J. He, T. J. Zhu, S. N. Zhang, X. B. Zhao, T. M. Tritt, *Appl. Phys. Lett.* **2008**, 93, 102109.
- [40] a) R. Venkatasubramanian, E. Siivola, T. Colpitts, B. O'Quinn, *Nature* **2001**, 413, 597. b) Q. Zhang, J. He, X. B. Zhao, S. N. Zhang, T. J. Zhu, H. Yin, T. M. Tritt, *J. Phys. D: Appl. Phys.* **2008**, 41, 185103. c) Q. Zhang, X. B. Zhao, H. Yin, T. J. Zhu, *J. Alloys. Compd.* **2008**, 464, 9. d) Y. Q. Cao, T. J. Zhu, X. B. Zhao, X. B. Zhang, J. P. Tu, *Appl. Phys. A* **2008**, 92, 321.
- [41] a) T. C. Harman, P. J. Taylor, M. P. Walsh, B. E. LaForge, *Science* **2002**, 297, 2229. b) W. J. Xie, X. F. Tang, Y. G. Yan, Q. J. Zhang, T. M. Tritt, *Appl. Phys. Lett.* **2009**, 94, 102111.
- [42] W. Kim, J. Zide, A. Gossard, D. Klenov, S. Stemmer, A. Shakouri, A. Majumdar, *Phys. Rev. Lett.* **2006**, 96, 045901.
- [43] A. I. Hochbaum, R. Chen, R. D. Delgado, W. Liang, E. C. Garnett, M. Najarian, A. Majumdar, P. Yang, *Nature* **2008**, 451, 163.
- [44] A. I. Boukai, Y. Bunimovich, J. Tahir-Kheli, J. K. Yu, W. A. Goddard, J. R. Heath, *Nature* **2008**, 451, 168.
- [45] D. Li, Y. Wu, P. Kim, L. Shi, P. Yang, A. Majumdar, *Appl. Phys. Lett.* **2003**, 83, 2934.
- [46] J. Zhou, Q. Jin, J. H. Seol, X. Li, L. Shi, *Appl. Phys. Lett.* **2005**, 87, 133109.
- [47] a) T. Yao, *Appl. Phys. Lett.* **1987**, 51, 1798. b) G. Chen, C. L. Tien, X. Wu, J. S. Smith, *J. Heat Transfer* **1994**, 116, 325. c) X. Y. Yu, G. Chen, A. Verma, J. S. Smith, *Appl. Phys. Lett.* **1995**, 67, 3554. d) G. Chen, C. L. Tien, *J. Thermophys. Heat Transfer* **1993**, 7, 311. e) S. Lee, D. Cahill, R. Venkatasubramanian, *Appl. Phys. Lett.* **1997**, 70, 2957.
- [48] H. Böttner, G. Chen, R. Venkatasubramanian, *MRS Bull.* **2006**, 31, 211.
- [49] J. P. Heremans, C. M. Thrush, D. T. Morelli, *Phys. Rev. B* **2004**, 70, 115334.
- [50] S. M. Lee, D. G. Cahill, R. Venkatasubramanian, *Appl. Phys. Lett.* **1997**, 70, 2957.
- [51] B. Yang, W. L. Liu, J. L. Liu, K. L. Wang, G. Chen, *Appl. Phys. Lett.* **2002**, 81, 3588.
- [52] Y. Zhang, J. Christofferson, A. Shakouri, D. Li, A. Majumdar, Y. Wu, R. Fan, P. Yang, *IEEE Trans. Nanotechnol.* **2006**, 5, 67.
- [53] B. Poudel, Q. Hao, Y. Ma, Y. C. Lan, A. Minnich, B. Yu, X. Yan, D. Z. Wang, A. Muto, D. Vashaee, X. Y. Chen, J. M. Liu, M. S. Dresselhaus, G. Chen, Z. F. Ren, *Science* **2008**, 320, 634.

- [54] G. Joshi, H. Lee, Y. C. Lan, X. W. Wang, G. H. Zhu, D. Z. Wang, R. W. Gould, D. C. Cuff, M. Y. Tang, M. S. Dresselhaus, G. Chen, Z. F. Ren, *Nano Lett.* **2008**, *8*, 4670.
- [55] Y. Ma, Q. Hao, B. Poudel, Y. C. Lan, B. Yu, D. Z. Wang, G. Chen, Z. F. Ren, *Nano Lett.* **2008**, *8*, 2580.
- [56] X. W. Wang, H. Lee, Y. C. Lan, G. H. Zhu, G. Joshi, D. Z. Wang, J. Yang, A. J. Muto, M. Y. Tang, J. Klatsky, S. Song, M. S. Dresselhaus, G. Chen, Z. F. Ren, *Appl. Phys. Lett.* **2008**, *93*, 193121.
- [57] G. H. Zhu, H. Lee, Y. C. Lan, X. W. Wang, G. Joshi, D. Z. Wang, J. Yang, D. Vashae, H. Guilbert, A. Pillitteri, M. S. Dresselhaus, G. Chen, Z. F. Ren, *Phys. Rev. Lett.* **2009**, *102*, 196803.
- [58] Z. F. Ren, B. Poudel, Y. Ma, Q. Hao, Y. C. Lan, A. Minnich, A. Muto, J. Yang, B. Yu, X. Yan, D. Z. Wang, J. M. Liu, M. S. Dresselhaus, G. Chen, *Mater. Res. Soc. Symp. Proc.* **2009**, *1166*, 1166-N04-03.
- [59] S. Bhattacharya, A. L. Pope, R. T. Litterton, T. M. Tritt, V. Ponnambalam, Y. Xia, S. J. Poon, *Appl. Phys. Lett.* **2000**, *77*, 2476.
- [60] J. P. Heremans, C. M. Thrush, D. T. Morelli, *J. Appl. Phys.* **2005**, *98*, 063703.
- [61] J. M. O. Zide, D. Vashae, Z. X. Bian, G. Zeng, J. E. Bowers, A. Shakouri, A. C. Gossard, *Phys. Rev. B* **2006**, *74*, 205335.
- [62] H. Ohta, S. Kim, Y. Mune, T. Mizoguchi, K. Nomura, S. Ohta, T. Nomura, Y. Nakanishi, Y. Ikuhara, M. Hirano, H. Hosono, K. Koumoto, *Nat. Mater.* **2007**, *6*, 129.
- [63] a) J. P. Heremans, V. Jovovic, E. S. Toberer, A. Saramat, K. Kurosaki, A. Charoenphakdee, S. Yamanaka, G. J. Snyder, *Science* **2008**, *321*, 554. b) B. Yu, H. Wang, B. Poudel, K. McEnaney, G. Chen, Z. Ren, *Thermoelectric Figure-of-Merit in Bulk p-type PbTe*, presented at APS March Meeting, Pittsburgh, PA, March **2009**. c) G. D. Mahan, J. O. Sofo, *Proc. Natl. Acad. Sci. USA* **1996**, *93*, 7436.
- [64] M. Dresselhaus, G. Dresselhaus, X. Sun, Z. Zhang, S. Cronin, T. Koga, *Phys. Solid State* **1999**, *41*, 679.
- [65] M. S. Dresselhaus, G. Chen, M. Y. Tang, R. G. Yang, H. Lee, D. Wang, Z. F. Ren, J. P. Fleurial, P. Gogna, *Mater. Res. Soc. Symp. Proc.* **2006**, *886*, 0886-F01-01.1.
- [66] a) H. Ni, T. Zhu, X. Zhao, *Physica B* **2005**, *364*, 50. b) T. J. Zhu, Y. Q. Liu, X. B. Zhao, *Mater. Res. Bull.* **2008**, *43*, 2850.
- [67] a) W. Z. Wang, B. Poudel, J. Yang, D. Z. Wang, Z. F. Ren, *J. Am. Chem. Soc.* **2005**, *127*, 13792. b) J. L. Mi, X. B. Zhao, T. J. Zhu, J. P. Tu, *Mater. Lett.* **2008**, *62*, 2363. c) Y. Q. Cao, T. J. Zhu, X. B. Zhao, *J. Alloys. Compd.* **2008**, *449*, 109.
- [68] W. Z. Wang, B. Poudel, D. Z. Wang, Z. F. Ren, *Adv. Mater.* **2005**, *17*, 2110.
- [69] B. Poudel, W. Z. Wang, D. Z. Wang, J. Y. Huang, Z. F. Ren, *J. Nanosci. Nanotechnol.* **2006**, *6*, 1050.
- [70] W. Z. Wang, X. Yan, B. Poudel, Y. Ma, Q. Hao, J. Yang, G. Chen, Z. F. Ren, *J. Nanosci. Nanotechnol.* **2008**, *8*, 452.
- [71] Y. Q. Cao, X. B. Zhao, T. J. Zhu, X. B. Zhang, J. P. Tu, *Appl. Phys. Lett.* **2008**, *92*, 143106.
- [72] a) L. Bertini, C. Stiewe, M. Toprak, S. Williams, D. Platzek, A. Mrotzek, Y. Zhang, C. Gatti, E. Müller, M. Muhammed, M. Rowe, *J. Appl. Phys.* **2003**, *93*, 438. b) T. Sun, X. B. Zhao, T. J. Zhu, J. P. Tu, *Mater. Lett.* **2006**, *60*, 2534.
- [73] a) J. Martin, G. S. Nolas, W. Zhang, L. Chen, *Appl. Phys. Lett.* **2007**, *90*, 222112. b) Y. Y. Zheng, T. J. Zhu, X. B. Zhao, J. P. Tu, G. S. Cao, *Mater. Lett.* **2005**, *59*, 2886.
- [74] K. Sridhar, K. Chattopadhyay, *J. Alloy. Compd.* **1998**, *264*, 293.
- [75] R. Martin-Lopez, A. Dauscher, H. Scherrer, J. Hejtmanek, H. Kenzari, B. Lenoir, *Appl. Phys. A: Mater. Sci. Process.* **1999**, *68*, 597.
- [76] J. Schilz, M. Riffel, K. Pixius, H. J. Meyer, *Powder Technol.* **1999**, *105*, 149.
- [77] K. Kishimoto, T. Koyanagi, *J. Appl. Phys.* **2002**, *92*, 2544.
- [78] S. S. Kim, S. Yamamoto, T. Aizawa, *J. Alloy. Compd.* **2004**, *375*, 107.
- [79] J. Yang, X. Fan, R. Chen, W. Zhu, S. Bao, X. Duan, *J. Alloy. Compd.* **2006**, *416*, 270.
- [80] J. Yang, R. Chen, X. Fan, S. Bao, W. Zhu, *J. Alloy. Compd.* **2006**, *407*, 330.
- [81] H. Wang, J. F. Li, C. W. Nan, M. Zhou, W. Liu, B. P. Zhang, T. Kita, *Appl. Phys. Lett.* **2006**, *88*, 092104.
- [82] W. S. Liu, B. P. Zhang, J. F. Li, L. D. Zhao, *J. Phys. D: Appl. Phys.* **2007**, *40*, 566.
- [83] W. S. Liu, B. P. Zhang, L. D. Zhao, J. F. Li, *Chem. Mater.* **2008**, *20*, 7526.
- [84] M. Zakeri, M. Allahkarami, G. Kavei, A. Khanmohammadian, M. Rahimpour, *J. Mater. Process. Technol.* **2009**, *209*, 96.
- [85] C. Suryanarayana, *Prog. Mater. Sci.* **2001**, *46*, 1.
- [86] P. S. Gilman, J. S. Benjamin, *Annu. Rev. Mater. Res.* **1983**, *13*, 279.
- [87] R. Davis, C. Koch, *Scripta Metall.* **1987**, *21*, 305.
- [88] C. C. Koch, *Annu. Rev. Mater. Res.* **1989**, *19*, 121.
- [89] H. Li, X. F. Tang, X. L. Su, Q. J. Zhang, *Appl. Phys. Lett.* **2008**, *92*, 202114.
- [90] T. Kumpeerapun, H. Scherrer, J. Khedari, J. Hirunlabh, S. Weber, A. Dauscher, B. Lenoir, B. Zighmati, H. M. Jahed, V. Kosalathip, in Proceedings of 25th International Conference on Thermoelectrics, Vienna, Austria **2006**, pp. 136–140.
- [91] J. Peng, J. Yang, T. Zhang, X. Song, Y. Chen, *J. Alloy. Compd.* **2004**, *381*, 313.
- [92] S. C. Ur, I. H. Kim, P. Nash, *J. Mater. Sci.* **2007**, *42*, 2143.
- [93] C. J. Liu, H. Yamauchi, *Phys. Rev. B* **1995**, *51*, 11826.
- [94] J. L. Harringa, B. A. Cook, *Mater. Sci. Eng. B* **1999**, *60*, 137.
- [95] Z. He, C. Stiewe, D. Platzek, G. Karpinski, E. Müller, S. Li, M. Toprak, M. Muhammed, *J. Appl. Phys.* **2007**, *101*, 053713.
- [96] J. M. Schultz, J. P. McHugh, W. A. Tiller, *J. Appl. Phys.* **1962**, *33*, 2443.
- [97] R. Lefever, G. McVay, R. Baughman, *Mater. Res. Bull.* **1974**, *9*, 863.
- [98] N. Savvides, H. J. Goldsmid, *J. Mater. Sci.* **1980**, *15*, 594.
- [99] J. F. Miller, R. C. Himes, *J. Electrochem. Soc.* **1960**, *107*, 915.
- [100] S. K. Bux, R. G. Blair, P. K. Gogna, H. Lee, G. Chen, M. S. Dresselhaus, R. B. Kaner, J. P. Fleurial, *Adv. Funct. Mater.* **2009**, *19*, 2445.
- [101] J. Yang, T. Aizawa, A. Yamamoto, T. Ohta, *J. Alloy. Compd.* **2000**, *309*, 225.
- [102] H. C. Kim, T. S. Oh, D. B. Hyun, *J. Phys. Chem. Solids* **2000**, *61*, 743.
- [103] X. Tang, W. Xie, H. Li, W. Zhao, Q. Zhang, M. Niino, *Appl. Phys. Lett.* **2007**, *90*, 012102.
- [104] M. Toprak, C. Stiewe, D. Platzek, S. Williams, L. Bertini, E. Müller, C. Gatti, Y. Zhang, M. Rowe, M. Muhammed, *Adv. Funct. Mater.* **2004**, *14*, 1189.
- [105] J. Yang, Q. Hao, H. Wang, Y. C. Lan, Q. Y. He, D. Z. Wang, J. A. Harriman, V. M. Varki, M. S. Dresselhaus, G. Chen, Z. F. Ren, *Phys. Rev. B*, **2009**, *80*, 115329.
- [106] G. S. Nolas, M. Kaeser, R. T. Littleton, IV, T. M. Tritt, *Appl. Phys. Lett.* **2000**, *77*, 1855.
- [107] Q. Y. He, Q. Hao, X. W. Wang, J. Yang, Y. C. Lan, X. Yan, B. Yu, Y. Ma, B. Poudel, G. Joshi, D. Z. Wang, G. Chen, Z. F. Ren, *J. Nanosci. Nanotechnol.* **2008**, *8*, 4003.
- [108] Q. Y. He, S. J. Hu, X. G. Tang, Y. C. Lan, J. Yang, X. W. Wang, Z. F. Ren, Q. Hao, G. Chen, *Appl. Phys. Lett.* **2008**, *93*, 042108.
- [109] S. C. Ur, J. C. Kwon, I. H. Kim, *J. Alloy. Compd.* **2007**, *442*, 358.
- [110] S. C. Ur, J. C. Kwon, I. H. Kim, *Met. Mater. Int.* **2008**, *14*, 625.
- [111] J. Yang, Y. Chen, W. Zhu, S. Bao, J. Peng, X. Fan, *J. Phys. D: Appl. Phys.* **2005**, *38*, 3966.
- [112] S. Bao, J. Yang, W. Zhu, X. Fan, X. Duan, J. Peng, *Mater. Lett.* **2006**, *60*, 2029.
- [113] S. Bao, J. Yang, J. Peng, W. Zhu, X. Fan, X. Song, *J. Alloy. Compd.* **2006**, *421*, 105.
- [114] K. Cai, E. Mueller, C. Drasar, C. Stiewe, *Solid State Commun.* **2004**, *131*, 325.
- [115] Z. He, D. Platzek, C. Stiewe, H. Chen, G. Karpinski, E. Müller, *J. Alloy. Compd.* **2007**, *438*, 303.
- [116] R. Song, T. Aizawa, J. Sun, *Mater. Sci. Eng. B* **2007**, *136*, 111.
- [117] R. B. Song, Y. Z. Liu, T. Aizawa, *Phys. Status Solidi RRL* **2007**, *1*, 226.
- [118] S. Bhattacharya, Y. Xia, V. Ponnambalam, S. J. Poon, N. Thadani, T. M. Tritt, *Mat. Res. Soc. Symp. Proc.* **2002**, *691*, G7.1.1.
- [119] Q. Y. He, Q. Hao, G. Chen, B. Poudel, X. W. Wang, D. Z. Wang, Z. F. Ren, *Appl. Phys. Lett.* **2007**, *91*, 052505.
- [120] J. Cui, X. Liu, W. Yang, D. Chen, H. Fu, P. Ying, *J. Appl. Phys.* **2009**, *105*, 063703.
- [121] M. Ito, T. Tada, S. Katsuyama, *J. Alloy. Compd.* **2003**, *350*, 296.

- [122] M. Ito, T. Tada, S. Hara, *J. Alloy. Compd.* **2006**, 408–412, 363.
- [123] H. Ni, X. Zhao, T. Zhu, X. Ji, J. Tu, *J. Alloy. Compd.* **2005**, 397, 317.
- [124] J. S. Lee, T. S. Oh, D. B. Hyun, *J. Mater. Sci.* **2000**, 35, 881.
- [125] X. A. Fan, J. Y. Yang, Z. Xie, K. Li, W. Zhu, X. K. Duan, C. J. Xiao, Q. Q. Zhang, *J. Phys. D: Appl. Phys.* **2007**, 40, 5975.
- [126] K. F. Cai, C. W. Nan, Y. Paderno, D. S. McLachlan, *Solid State Commun.* **2000**, 115, 523.
- [127] D. M. Rowe, R. W. Bunce, *J. Phys. D: Appl. Phys.* **1969**, 2, 1497.
- [128] C. B. Murray, C. R. Kagan, M. G. Bawendi, *Annu. Rev. Mater. Sci.* **2000**, 30, 545.
- [129] Y. C. Lan, B. Poudel, Y. Ma, D. Z. Wang, M. S. Dresselhaus, G. Chen, Z. F. Ren, *Nano Lett.* **2009**, 9, 1419.
- [130] D. Medlin, G. Snyder, *Curr. Opin. Colloid Interface Sci.* **2009**, 14, 226.
- [131] J. Yang, T. Aizawa, A. Yamamoto, T. Ohta, *Mater. Chem. Phys.* **2001**, 70, 90.
- [132] N. Miyashita, T. Yano, R. Tsukuda, I. Yashima, *J. Ceram. Soc. Jpn.* **2003**, 111, 386.
- [133] H. J. Im, D. H. Kim, T. Mitani, K. C. Je, *Jpn. J. Appl. Phys.* **2004**, 43, 1094.
- [134] X. Fan, J. Yang, R. Chen, W. Zhu, S. Bao, *Mater. Sci. Eng. A* **2006**, 438–440, 190.
- [135] X. Zhao, S. Yang, Y. Cao, J. Mi, Q. Zhang, T. Zhu, *J. Electron. Mater.* **2009**, 38, 1017.
- [136] I. Yashima, H. Watanabe, T. Ogisu, R. Tsukuda, S. Sato, *Jpn. J. Appl. Phys.* **1998**, 37, 2472.
- [137] J. Seo, K. Park, D. Lee, C. Lee, *Mater. Sci. Eng. B* **1997**, 49, 247.
- [138] G. A. Slack, M. A. Hussain, *J. Appl. Phys.* **1991**, 70, 2694.
- [139] B. Abeles, *Phys. Rev.* **1963**, 131, 1906.
- [140] N. K. Abrikosov, V. S. Zemsikov, E. K. Iordanishvili, A. V. Petrov, V. V. Rozhdestvenskaya, *Sov. Phys. Semicond.* **1968**, 2, 1762.
- [141] J. P. Dismukes, L. Ekstrom, E. F. Steigmeier, I. Kudman, D. S. Beers, *J. Appl. Phys.* **1964**, 35, 2899.
- [142] C. M. Bhandari, D. M. Rowe, *Contemp. Phys.* **1980**, 21, 219.
- [143] M. Abdellaoui, E. Gaffet, *J. Phys. IV France* **1994**, 4, C3-291.
- [144] E. Gaffet, L. Yousfi, *Mater. Sci. Forum* **1992**, 88–90, 51.
- [145] H. Bakker, L. M. Di, *Mater. Sci. Forum* **1994**, 88–90, 27.
- [146] D. M. Rowe, *J. Phys. D: Appl. Phys.* **1974**, 7, 1843.
- [147] a) B. C. Sales, D. Mandrus, R. K. Williams, *Science* **1996**, 272, 1325. b) J. L. Mi, X. B. Zhao, T. J. Zhu, J. P. Tu, *J. Phys. D: Appl. Phys.* **2008**, 41, 205403. c) J. L. Mi, X. B. Zhao, T. J. Zhu, J. Ma, *J. Alloys. Compd.* **2008**, 452, 225. d) J. L. Mi, X. B. Zhao, T. J. Zhu, J. P. Tu, *Appl. Phys. Lett.* **2007**, 91, 172116. e) H. Li, X. Tang, Q. Zhang, *J. Electronic Mater.* **2009**, 38, 1224. f) X. F. Tang, H. Li, Q. J. Zhang, M. Niino, T. Goto, *J. Appl. Phys.* **2006**, 100, 123702.
- [148] a) G. S. Nolas, J. L. Cohn, G. A. Slack, *Phys. Rev. B* **1998**, 58, 164. b) Y. Z. Pei, J. Yang, L. D. Chen, W. Zhang, J. R. Salvador, J. Yang, *Appl. Phys. Lett.* **2009**, 95, 042101. c) S. Q. Bai, Y. Z. Pei, L. D. Chen, W. Q. Zhang, X. Y. Zhao, J. Yang, *Acta Mater.* **2009**, 57, 3135. d) Y. Z. Pei, S. Q. Bai, X. Y. Zhao, W. Zhang, L. D. Chen, *Solid State Sci.* **2008**, 10, 1422. e) X. Y. Zhao, X. Shi, L. D. Chen, W. Q. Zhang, S. Q. Bai, Y. Z. Pei, X. Y. Li, T. Goto, *Appl. Phys. Lett.* **2006**, 89, 092121. f) X. F. Tang, Q. J. Zhang, L. D. Chen, T. Goto, T. Hirai, *J. Appl. Phys.* **2005**, 97, 093712.
- [149] a) C. Uher, in *Advances in Thermoelectric Materials I*, Vol. 69 (Ed.: T. Tritt), Academic Press, New York **2001**, pp. 139–253; b) Z. G. Mei, J. Yang, Y. Z. Pei, W. Zhang, L. D. Chen, J. Yang, *Phys. Rev. B* **2008**, 77, 045202. c) X. Shi, L. D. Chen, S. Q. Bai, X. Y. Huang, X. Y. Zhao, Q. Yao, U. Uher, *J. Appl. Phys.* **2007**, 102, 103709. d) X. Y. Zhao, X. Shi, L. D. Chen, W. Q. Zhang, W. B. Zhang, Y. Z. Pei, *J. Appl. Phys.* **2006**, 99, 053711. e) X. Y. Li, L. D. Chen, J. F. Fan, W. B. Zhang, T. Kawahara, T. Hirai, *J. Appl. Phys.* **2005**, 98, 083702. f) X. F. Tang, L. D. Chen, J. Wang, Q. J. Zhang, T. Goto, T. Hirai, *J. Alloys Compd.* **2005**, 394, 259.
- [150] T. Caillat, A. Borshchevsky, J. P. Fleurial, *J. Appl. Phys.* **1996**, 80, 4442.
- [151] B. Chen, J. H. Xu, C. Uher, D. T. Morelli, G. P. Meisner, J. P. Fleurial, T. Caillat, A. Borshchevsky, *Phys. Rev. B* **1997**, 55, 1476.
- [152] V. Keppens, D. Mandrus, B. C. Sales, B. C. Chakoumakos, P. Dai, R. Coldea, M. B. Maple, D. A. Gajewski, E. J. Freeman, S. Bennington, *Nature* **1998**, 395, 876.
- [153] M. Puyet, B. Lenoir, A. Dauscher, M. Dehmas, C. Stiewe, E. Muller, *J. Appl. Phys.* **2004**, 95, 4852.
- [154] L. D. Chen, T. Kawahara, X. F. Tang, T. Goto, T. Hirai, J. S. Dyck, W. Chen, C. Uher, *J. Appl. Phys.* **2001**, 90, 1864.
- [155] H. Y. Geng, S. Ochi, J. Q. Guo, *Appl. Phys. Lett.* **2007**, 91, 022106.
- [156] J. Yang, Y. Chen, J. Peng, X. Song, W. Zhu, J. Su, R. Chen, *J. Alloy. Compd.* **2004**, 375, 229.
- [157] S. Bao, J. Yang, X. Song, J. Peng, W. Zhu, X. Fan, X. Duan, *Mater. Sci. Eng. A* **2006**, 438–440, 186.
- [158] S. C. Ur, I. H. Kim, *Mater. Lett.* **2002**, 57, 543.
- [159] X. Shi, H. Kong, C. P. Li, C. Uher, J. Yang, J. R. Salvador, H. Wang, L. Chen, W. Zhang, *Appl. Phys. Lett.* **2008**, 92, 182101.
- [160] H. Li, X. F. Tang, Q. J. Zhang, C. Uher, *Appl. Phys. Lett.* **2008**, 93, 252109.
- [161] B. C. Sales, D. Mandrus, B. C. Chakoumakos, V. Keppens, J. R. Thompson, *Phys. Rev. B* **1997**, 56, 15081.
- [162] X. Song, J. Yang, J. Peng, Y. Chen, W. Zhu, T. Zhang, *J. Alloy. Compd.* **2005**, 399, 276.
- [163] S. Bao, J. Yang, W. Zhu, X. Fan, X. Duan, *J. Alloy. Compd.* **2009**, 476, 802.
- [164] W. Xu, L. Li, R. Huang, M. Zhou, L. Zheng, L. Gong, C. Song, *Front. Energy Power Eng. China* **2009**, 3, 90.
- [165] R. J. Huang, L. F. Li, W. Xu, L. H. Gong, *Solid State Commun.* **2009**, 149, 1633.
- [166] K. F. Cai, C. W. Nan, M. Schmuecker, E. Mueller, *J. Alloy. Compd.* **2003**, 350, 313.
- [167] G. J. Snyder, M. Christensen, E. Nishibori, T. Caillat, B. B. Iversen, *Nat. Mater.* **2004**, 3, 458.
- [168] C. Chiriac, D. G. Cahill, N. Nguyen, D. Johnson, A. Bodapati, P. Keblinski, P. Zschack, *Science* **2007**, 315, 351.
- [169] A. S. Henry, G. Chen, *J. Comput. Theor. Nanosci.* **2008**, 5, 141.
- [170] J. Callaway, *Phys. Rev.* **1959**, 113, 1046.
- [171] E. F. Steigmeier, B. Abeles, *Phys. Rev.* **1964**, 136, A1149.
- [172] D. T. Morelli, V. Jovovic, J. P. Heremans, *Phys. Rev. Lett.* **2008**, 101, 035901.
- [173] P. L. Kapitza, *J. Phys. (USSR)* **1941**, 4, 181.
- [174] E. Schwartz, R. Pohl, *Rev. Mod. Phys.* **1989**, 61, 605.
- [175] G. Chen, *J. Heat Transfer* **1997**, 119, 220.
- [176] G. Chen, T. Zeng, *Microscale Thermophys. Eng.* **2001**, 5, 71.
- [177] R. Prasher, *Int. J. Heat Mass Tran.* **2005**, 48, 4942.
- [178] H. Zhong, J. R. Lukes, *Phys. Rev. B* **2006**, 74, 125403.
- [179] A. Minnich, G. Chen, *Appl. Phys. Lett.* **2007**, 91, 073105.
- [180] A. Khitun, K. L. Wang, G. Chen, *Nanotechnology* **2000**, 11, 327.
- [181] Z. Neil, R. L. Jennifer, *Phys. Rev. B* **2008**, 77, 094302.
- [182] G. A. Slack in *Solid State Physics*, Vol. 34 (Eds: F. Seitz, D. Turnbull, H. Ehrenreich), Academic Press, New York **1979**, pp. 1–71.
- [183] D. G. Cahill, S. K. Watson, R. O. Pohl, *Phys. Rev. B* **1992**, 46, 6131.
- [184] A. J. Minnich, M. S. Dresselhaus, Z. F. Ren, G. Chen, *Energy Environ. Sci.* **2009**, 2, 466.